Transport structure of the South Atlantic Ocean derived from a high-resolution numerical model and observations

Xiaobiao Xu[1], Eric P. Chassignet[1], Shenfu Dong[2], and Molly O'Neill Baringer[3]

[1]Florida State University
[2]NOAA/AOML
[3]NOAA AOML

November 24, 2022

Abstract

The South Atlantic Ocean plays an important role in the Atlantic meridional overturning circulation (AMOC), connecting it to the Indian and Pacific Oceans as part of the global overturning circulation system; yet the detailed time mean circulation structure in this region and the large-scale spatial pattern of the AMOC variability remain unclear. Using model outputs from a 60-year, eddying global ocean-sea ice simulation validated against observations at a zonal section at 34°S, a meridional section at 65°W in the Drake Passage, and a meridional section southwest of Africa, we show that the upper limb of the AMOC originates primarily from the Agulhas leakage and that, while the cold Pacific water from the Drake Passage does not contribute significantly to the AMOC, it does play a role in setting the temperature and salinity properties of the water masses in the subtropical South Atlantic. We also find that the North Atlantic deep water (NADW) in the lower limb of the AMOC flows southward as a deep western boundary current all the way to 45°S and then turns eastward to flow across the Mid-Atlantic Ridge near 42°S, and that the recirculation around the Vitoria-Trindade seamount chain brings some NADW into the Brazil Basin interior. Finally, we find that the modeled AMOC variability is coherent on interannual to decadal timescales from 35°S to about 35°N, where diapycnal water mass transformations between the upper and lower limbs of the AMOC are expected to be small.

Transport structure of the South Atlantic Ocean derived from a high-resolution numerical model and observations

Xiaobiao Xu*

COAPS/Florida State University, Tallahassee, Florida

Eric P. Chassignet

COAPS/Florida State University, Tallahassee, Florida

Shenfu Dong

AOML/National Oceanic and Atmospheric Administration, Miami, Florida

Molly O. Baringer

AOML/National Oceanic and Atmospheric Administration, Miami, Florida

Corresponding author: Xiaobiao Xu (xxu3@fsu.edu)

2000 Levy Avenue, Building A, Tallahassee FL 30306

Key Points:

1. The upper limb of the AMOC originates primarily from the warm Indian Ocean water through the Agulhas Leakage
2. The NADW in the lower limb of AMOC flows southward as a DWBC to 45°S and then turns eastward to flow across the Mid-Atlantic Ridge near 42°S
3. The AMOC variability is latitudinally coherent from 35°S to about 35°N at interannual to decadal timescales

Abstract

The South Atlantic Ocean plays an important role in the Atlantic meridional overturning circulation (AMOC), connecting it to the Indian and Pacific Oceans as part of the global overturning circulation system; yet the detailed time mean circulation structure in this region and the large-scale spatial pattern of the AMOC variability remain unclear. Using model outputs from a 60-year, eddying global ocean-sea ice simulation validated against observations at a zonal section at 34°S, a meridional section at 65°W in the Drake Passage, and a meridional section southwest of Africa, we show that the upper limb of the AMOC originates primarily from the Agulhas leakage and that, while the cold Pacific water from the Drake Passage does not contribute significantly to the AMOC, it does play a role in setting the temperature and salinity properties of the water masses in the subtropical South Atlantic. We also find that the North Atlantic deep water (NADW) in the lower limb of the AMOC flows southward as a deep western boundary current all the way to 45°S and then turns eastward to flow across the Mid-Atlantic Ridge near 42°S, and that the recirculation around the Vitoria-Trindade seamount chain brings some NADW into the Brazil Basin interior. Finally, we find that the modeled AMOC variability is coherent on interannual to decadal timescales from 35°S to about 35°N, where diapycnal water mass transformations between the upper and lower limbs of the AMOC are expected to be small.

Plain Language Summary

The Atlantic Ocean features a meridional overturning circulation in which the warm water flows northward in the upper layer and cold water flows southward in the deep. Through South Atlantic this overturning circulation is connected to the Indian/Pacific Oceans and becomes part of the global circulation system. The spatial structure and temporal variability of the South Atlantic circulation remain not well-determined in observations, however, and in this study, we used a

numerical model that represented well the observed volume transports at key locations to address the questions. We showed that the northward-flowing branch of the overturning circulation originates primarily from the Indian (Ocean) water; the Pacific water does flow into the subtropical South Atlantic and modifies the temperature and salinity property there. The deep water flows southward along western boundary all the way to about 45°S and then turns eastward to flow across the Mid-Atlantic Ridge near 42°S; some deep water also enters the interior of the Brazil Basin through eddies and recirculation. The variability of the overturning circulation on interannual to decadal timescales correlates in a wide latitudinal range from 35°S to 35°N, away from the high-latitude regions where the deep water is formed and upwelled.

1. Introduction

In the Atlantic Ocean, warm water from the South Atlantic flows northward in approximately the upper 1000 meters, loses buoyancy to the atmosphere by cooling *en route* to the northern North Atlantic, and eventually sinks and returns southward at depth as the cold North Atlantic Deep Water (NADW). The temperature difference between the upper and lower limbs of this Atlantic meridional overturning circulation (AMOC) leads to a large northward oceanic heat transport throughout the entire Atlantic basin, in contrast to the poleward heat transport in the Indo-Pacific Ocean (e.g., Macdonald and Baringer, 2013). The South Atlantic Ocean, defined here as the area south of 20°S (Figure 1), plays an important role in that it is through this region where the upper and lower AMOC limbs are connected to the Indian and Pacific Oceans and are entangled in the global overturning circulation system (e.g., Gordon, 1986; Broecker, 1991; Schmitz, 1995, 1996; Richardson, 2008; Talley, 2013). Thus, a comprehensive knowledge of the circulation in this region is essential to our understanding of the spatial structure and temporal variability of the AMOC.

Significant observations have been made in the last 15 years or so toward quantifying and monitoring the AMOC in the South Atlantic, particularly along a latitude near 34.5°S (e.g., Baringer and Garzoli, 2007; Dong et al., 2009, 2014, 2015; Garzoli et al., 2013; Goes et al., 2015; Meinen et al., 2013, 2018). These observations, which consist of moorings, expendable Bathythermograph (XBT), and Argo float measurements, yield a time mean AMOC transport on the order of 14-20 Sv. They also show that there is significant AMOC variability on several timescales, similar to that observed by the RAPID array at 26.5°N (e.g., Smeed et al., 2018). Beyond 34.5°S, however, the observations in the South Atlantic remain sparse and short (in time). Overall, our understanding of the spatial structure of the time mean circulation is mostly limited to the schematic of Stramma and England (1999) and even less is known about its temporal variability.

In particular, there is a long-standing debate regarding the source of the upper limb of the AMOC (Gordon, 2001): whether it originates from the warm, saline Indian waters through the southern rim of Africa (e.g., Gordon 1986; Saunders and King 1995) or from the cooler, fresher Pacific water through the Drake Passage (e.g., Rintoul, 1991; Schlitzer, 1996). Although recent studies seem to favor the warm-water route from the Indian Ocean through the Agulhas leakage (e.g., Richardson 2007; Beal et al., 2011), the relative contributions of cold versus warm water are still uncertain (Garzoli and Matano, 2011; Bower et al., 2019). For example, Rodrigues et al. (2010) estimated a cold-water contribution of 4.7 Sv based on quasi-isobaric subsurface floats and hydrographic data. This value is similar to the recent estimate by Rühs et al. (2019) from a Lagrangian analysis of an eddy-rich model, but it is significantly higher than the historical estimates of 1-2 Sv estimated from Lagrangian analyses in models or reanalysis (e.g., Speich et al., 2001; Donners and Drijfhout, 2004; Friocourt et al., 2005; Rousselet et al., 2020). At depth, in

92 the lower limb of the AMOC, much attention has been paid to an eastward flow of the NADW
93 near 22°S (e.g., Speer et al., 1995; Stramma and England, 1999; Arhan et al., 2003; Hogg and
94 Thurnherr, 2005; van Sebille et al., 2012; Garzoli et al., 2015). However, the extent of the eastward
95 penetration in the Angola basin and the exact location where the DWBC turns eastward south of
96 34°S and flows across the Mid-Atlantic Ridge (MAR) are still debatable. Finally, there is also the
97 underlying question as to whether the AMOC variability is meridionally coherent throughout the
98 whole Atlantic (Kelly et al., 2004; Xu et al., 2014).

99 Three-dimensional circulation information beyond the existing observations is required in order to
100 address the above questions. In this paper, we use a high-resolution numerical model to investigate
101 in detail the structure of the mean circulation in the South Atlantic as well as the temporal
102 variability of the AMOC on basin scales. The paper is structured as follows: Section 2 summarizes
103 the basic features of the numerical simulation. Section 3 compares the modeled large-scale
104 circulation pattern and the circulation structure with observations at three key observation
105 locations: 34°S across the South Atlantic, 65°W in the Drake Passage, and along a Prime Meridian-
106 Good Hope section southwest of Africa (Figure 1). The model results are shown to be in good
107 agreement with the observed transports and are then used to document the time mean circulation
108 pattern in the South Atlantic (Section 4) and the latitudinal coherence of the AMOC variability
109 throughout the Atlantic basin (Section 5). Summary and discussions follow in Section 6.

110 **2. Numerical Simulation**

111 The numerical results presented in this study are from a long-term global ocean-sea ice hindcast
112 simulation performed using the Hybrid Coordinate Ocean Model (HYCOM, Bleck, 2002;
113 Chassignet et al., 2003), coupled with the Community Ice CodE (CICE, Hunke and Lipscomb,
114 2008). The vertical coordinate of the HYCOM is isopycnic in the stratified open ocean and makes

115 a dynamically smooth and time-dependent transition to terrain following in the shallow coastal
116 regions and to fixed pressure levels in the surface mixed layer and/or unstratified seas. In doing
117 so, the model combines the advantages of the different coordinate types in simulating coastal and
118 open ocean circulation features simultaneously (e.g., Chassignet et al., 2006).

119 The simulation has a horizontal resolution of 1/12° (~6 km in the area of interest) and a vertical
120 resolution of 36 layers (in σ_2). It is initialized using the January temperature and salinity from an
121 ocean climatology (Carnes, 2009) and is forced using the latest surface-atmospheric reanalysis
122 dataset JRA55 (Tsujino et al., 2018), which has a refined grid spacing of ~55 km and temporal
123 interval of 3 hours and covers the time period of 1958-2018. The surface heat flux forcing is
124 computed using the shortwave and longwave radiations from JRA55, as well as the latent and
125 sensible heat fluxes derived from the CORE bulk formulae of Large and Yeager (2004) and the
126 model sea surface temperature (SST). The surface freshwater forcing includes evaporation,
127 precipitation, and climatological river runoffs. In addition, the model sea surface salinity (SSS) is
128 restored toward ocean climatology with a restoring timescale of two months and it is constrained
129 by an ad hoc assumption of zero global net flux at each time step. The wind stress is calculated
130 from the atmospheric wind velocity and does not take into account the shear introduced by the
131 ocean currents. The simulation starts from rest and is integrated over 1958-2018 with no data
132 assimilation. The horizontal diffusion parameters are listed in Table 1. In this study, we focus on
133 the last 40 years of the simulation (1979-2018) as being representative of the time-mean circulation
134 after spin-up (see Figure 2 below).

135 While a detailed evaluation of the global ocean circulation and of the sea ice in the model is
136 provided in Chassignet and al. (2020), some basic measures are useful. Figure 2 displays the
137 evolution of the domain averaged potential temperature and total kinetic energy of the world ocean.

138 The model temperature exhibits a weak cooling of ~0.06° C per century from early 1960s to late
139 1990s, followed with a 20-year warming of ~0.11° C per century from 1998 to 2018 (Figure 2a,
140 domain-averaged salinity is constant because of the zero net freshwater flux constraint). The
141 modeled warming rate for the last 20 years corresponds to a positive net heat flux of ~0.50 W/m^2.
142 This net heat flux in model is comparable with the estimates of 0.50 (±0.43) W/m^2 based on the
143 energy gain at the top of atmosphere for 2001-2010 (Loeb et al., 2012) and 0.64 (±0.11) W/m^2
144 based on 0-700 m oceanic heat content change from combined XBT and Argo data for 1993-2008
145 (Roemmich et al., 2015). The modeled total kinetic energy spins up quickly to ~35 cm^2/s^2 in the
146 first two years and remains on that level for the rest of the integration (Figure 2b). The global 1/10°
147 simulation performed by Maltrud and McClean (2005) using the Parallel Ocean Program (POP)
148 also reaches a maximum in kinetic energy in the first couple of years and levels off for the rest of
149 the simulation, except that the energy level is slightly lower at 25-30 cm^2/s^2 (their Figure 1).

150 The sea ice is quantified and monitored in term of sea ice extent, defined as the area with 15% or
151 higher sea ice concentration. Figure 3 compares the evolution of the modeled sea ice extent in
152 million km^2 with the latest results from the National Snow and Ice Data Center (Fetterer et al.,
153 2017). There is a general agreement between model and data in both the northern and southern
154 hemispheres and on both seasonal (Figure 3a) and interannual (Figure 3b) timescales. In particular,
155 as in the observations, the modeled sea ice extent has been decreasing in the northern hemisphere
156 since the beginning of the observations in 1979. The modeled sea ice extent in the southern
157 hemisphere, despite having lower annual mean values than observed, is relatively stable or
158 increases slightly over time and the variability is in good agreement with the observations (Figure
159 3b).

Figure 4 shows the modeled AMOC transport at 26.5°N, defined as the northward trans-basin transport above the modeled time mean maximum overturning depth (1000 m). The modeled AMOC transport has a mean and standard value of 14.2 ± 3.1 Sv and exhibits a multidecadal variability, with low transport in 1970s and high transport in 1990s (Figure 4a). The modeled mean AMOC transport in 2004-2017 is 13.6 Sv, which is 3.7 Sv or ~20% lower than the 17.3 Sv based on the RAPID data (updated from Smeed et al., 2018). The modeled AMOC variability, however, compares well to the observations: On interannual timescales, the magnitude of the AMOC variability is lower in model than in the RAPID observations (standard deviation of 1.0 Sv versus 1.5 Sv), but the two have a similar time evolution that is also consistent with the meridional heat transport anomaly of Trenberth et al. (2019) based on independent observations (Figure 4b). On seasonal timescale, the modeled AMOC variability is similar to the RAPID observations in both magnitude (multi-year averaged monthly mean transports give a standard deviation of 1.6 Sv in both time series) and phase, with low transports in January-June and high transports in July-December (Figure 4c).

Table 1. Viscosity and diffusion coefficients used in the 1/12° global ocean simulation

Parameters	Values
Laplacian coefficient for momentum	20 m^2 s^{-1}
Biharmonic diffusive velocity for momentum	1 cm s^{-1}
Biharmonic diffusive velocity for layer thickness	1.5 cm s^{-1}
Laplacian diffusive velocity for tracers	0.5 cm s^{-1}

3. Model validation

In this section, we first evaluate the large-scale surface circulation and then quantify the modeled transport structure at three sections in the South Atlantic: 34°S, 65°W in the Drake Passage, and a Prime Meridian-Good Hope section southwest of Africa (Figure 1). Significant observations have been conducted at these locations and they provide a benchmark for evaluating the realism of the modeled transports, which will be used to document the transport structure of the South Atlantic in Section 4.

3.1 The surface circulation pattern

Figure 5 compares the observed and modeled mean sea surface height (SSH), SSH variability, and eddy kinetic energy (EKE) of the surface currents in the South Atlantic. The observed mean SSH (Figure 5a) is from the latest mean dynamic topography climatology CNES-CLS18 (Mulet et al. 2020) while the SSH variability (Figure 5c) and surface EKE (Figure 5e) are derived from the AVISO data over the 1993-2018 period, the same time period used for the model results. In the western side of the domain, part of the Antarctic Circumpolar Current (ACC) turns north after passing the Drake Passage and becomes the Malvinas Current (also called the Falkland Current). The latter continues to flow northward along the continental shelf of Argentina until it meets the southward flowing Brazil Current south of the Rio de la Plata estuary near 36°S. The confluence of these two western boundary currents with opposite directions and very different properties (warm salty subtropical water versus cold fresh subantarctic water) leads to numerous high-energy eddies and thus strong variability in this so-called Brazil-Malvinas confluence zone (Figures 5c-f). In the south, the ACC is mostly zonal and exhibits a contracted (stronger) front in two areas: one near 40°W south of the Zapiola Drift and the other near 10°W over the MAR. Overall, there is a good agreement between the model and the observations in the western and southern part of

199 the domain, with the exception of a slightly lower model SSH variability offshore in the Brazil-
200 Malvinas confluence zone near 40°S.

201 West of Africa, the model results exhibit a narrow tongue of high SSH variability/EKE that extends
202 farther northwest into the South Atlantic than in observations. This is a common feature for many
203 eddying models (e.g., Maltrud and McClean, 2005; Dong et al. 2011; van Sebille et al. 2012) where
204 the Agulhas rings that shed from the Agulhas retroflection and translate northwestward into the
205 South Atlantic follow a regular pathway and are too energetic. Plots of the SSH variability for both
206 the model and the observations along the Prime Meridian over the observational period of 1993-
207 2018 in Figure 6 show that the modeled rings are stronger and pass the Prime Meridian within a
208 smaller latitudinal range than in the observations.

209 **3.2 Transport across 34°S**

210 Figures 7a-d display a vertical section of the time-mean potential temperature θ and salinity S at
211 34°S. The observations are based on the gridded monthly Argo profiles (2004-2014) for the upper
212 2000 m and the World Ocean Atlas 2013 (WOA13, Locarnini et al. 2013; Zweng et al. 2013)
213 below 2000 m; the model results are 40-year means from 1979 to 2018. The water column at this
214 latitude can be divided into four density layers of water masses that are characterized most clearly
215 by its salinity (θ decreases monotonically): saline near surface water (σ_2<35.65 kg m^{-3}), fresh
216 Antarctic Intermediate Water (AAIW, 35.65<σ_2<36.58), saline NADW (36.58<σ_2<37.12), and
217 fresh Antarctic Bottom Water (AABW, σ_2>37.12). There is a good agreement in the θ and S
218 distributions, such as the warm/saline anomaly in 2000-3000 m depth range associated with the
219 NADW in the DWBC. For a more quantitative comparison, Figures 7e-f display the volumetric θ-
220 S diagram along 34°S for both observations and model results. The color shading is volume

221 percentage of water mass calculated with a $\Delta\theta\times\Delta$S grid resolution of 0.1°C×0.02 psu and the
222 circled black/red lines are the volume weighted θ-S values calculated for each of the HYCOM
223 density layers. AAIW occupies ~20% of the volume at this latitude in both the observations and
224 model results, and this water mass as a whole is 0.35°C warmer and 0.11 psu saltier in the model
225 than in observations (the maximum θ-S difference is ~0.8°C and 0.18 psu for an individual density
226 layer). Above the AAIW, the modeled near surface water is about 0.8°C warmer than observed
227 and its salinity is very close to the observations (error on the order of 0.02 psu); below the AAIW,
228 the model results exhibit more AABW and less NADW than in WOA13, but the differences in θ-
229 S properties are small (0.1°C and 0.02 psu, respectively). Overall, the modeled water properties
230 are consistent with observations.

231 The time mean meridional velocity across 34°S and the corresponding volume transports for the
232 four water masses defined above are shown in Figure 8. The observations consist of geostrophic
233 transports derived from θ/S profiles (Argo-WOA13 data) and Ekman transports from the wind
234 stress; see Dong et al. (2014) for details. The model results are 40-year means (1979-2018). The
235 main circulation at this latitude consists of the South Atlantic subtropical gyre (southward Brazil
236 Current near the western boundary and northward interior flow) and the AMOC (northward
237 Bengula Current near the eastern boundary and southward DWBC near the western boundary).
238 Quantitatively, the total transport of the southward western boundary current is about 42 Sv (12,
239 8, and 22 Sv for the surface water, AAIW, and NADW, respectively) in model, compared to 45
240 Sv (7, 8, and 30 Sv for the surface water, AAIW, and NADW, respectively) in observations. In the
241 surface water and AAIW layers, the observed subtropical gyre extends from the western boundary
242 to 0-10°E, while the northward-flowing AMOC component occupies the rest of the section to the
243 coast of Africa. The modeled transport pattern is similar to the observations, except that the regular

pathway of the Agulhas rings leads to a north/south circulation in the Cape Basin. In the NADW layer, both observations and model results show a strong southward DWBC west of 40°W and a northward return flow east of 40°W. Note that the DWBC is quite wide at this latitude and that the transport obtained by Meinen et al. (2017), 15 Sv west of 44.5°W, does not include the full DWBC (near 30 Sv in Argo-WOA13 based observations and 22 Sv in model). The return flow is mostly localized over the Walvis Ridge. In the Cape Basin, both the Argo-WOA13 based observations and the model show a recirculation of the NADW which is consistent with the recent results of Kersalé et al. (2019) derived from moored CPIES-Current and Pressure recording Inverted Echo Sounders. This deep recirculation is likely driven by eddy activity in the upper ocean and is stronger in the model (see Figure 5). The pattern does not appear to be affected by the fact that the modeled Agulhas eddies follow a regular pathway. The modeled AABW transport is about 2 Sv in the western basin, much less than the 4-7 Sv estimated in observations (e.g., Hogg et al., 1982; Speer and Zenk, 1993). There is no AABW transport in the Argo-WOA13 based results.

The meridional flows shown in Figure 8 have a significant barotropic component and the baroclinic nature of the AMOC, i.e., northward flows in the upper limb and southward flows in the lower limb, becomes apparent only when integrated across the basin (Figure 9). The zonally integrated mean transport streamfunction with respect to the depth z shows a maximum overturning depth near 1300 m in both observations and model results (Figure 9a). The modeled mean AMOC transport is 14.7 Sv. This value agrees with the recent SAMOC estimate based on six years of moored observations at the western and eastern boundaries (14.7 Sv, Meinen et al., 2018), but is significantly lower than the estimates based on XBT transects (18 Sv, Dong et al., 2009; Garzoli et al., 2013) and Argo-WOA13 (20 Sv, Dong et al., 2014). With respect to density (Figure 9b), the northward AMOC limb is above the density surface (σ_2) 36.58 kg/m^3 and the

267 southward limb below. The modeled mean AMOC transport in density space is 15.8 Sv, compared
268 to 18.7 Sv based on Argo-WOA13. The modeled northward AMOC limb consists of 9.0 Sv of
269 warm surface water transport and 6.8 Sv of AAIW transport, compared to 12.7 and 6.0 Sv,
270 respectively, in the Argo-WOA13 observations. This leads to a lower meridional heat transport
271 (MHT) of 0.36±0.23 PW in the model, compared to 0.68±0.24 PW in the Argo-WOA13
272 observations. The historical estimates of the MHT near this latitude are 0.22-0.62 PW (see Table
273 29.3 in Macdonald and Baringer, 2013).

274 At 34°S, the modeled AMOC transport variability is lower than in the observations on both
275 interannual and seasonal timescales (Figure 10): On interannual timescale, the model AMOC
276 transports have a standard deviation of 1.0 Sv in 2004-2014, compared to 1.9 Sv in Argo-WOA13
277 based observations for the same period and 2.6 Sv in SAMOC results (Meinen et al., 2018) for a
278 shorter, 6-year period (2009-2010 and 2013-2017). The time evolution of the modeled AMOC
279 variability is similar to the Argo-WOA13 based observations in 2004-2012 but differ after 2012
280 (Figure 10a); note the Argo-WOA13 and SAMOC observations also differ in 2013-2014 when the
281 two observations overlap. On seasonal timescale, the modeled AMOC transports have a standard
282 deviation of 2.2 Sv, compared to 3.3 Sv in the Argo-WOA13 and 2.9 Sv in the SAMOC
283 observations. Although the magnitude is lower, the phase of the modeled seasonal variability is
284 consistent with the Argo-WOA13 and the SAMOC based observations (Figure 10b).

285 **3.3 Transport through the Drake Passage at 65°W**

286 The Drake Passage is an ACC chokepoint and the place where long-term sustained monitoring
287 programs have been conducted; see Meredith et al. (2011) for a review of historical observations.
288 The canonical full-depth volume transport is 133.8 ±11.2 Sv, based on year-long current meter
289 mooring and cruise data obtained during the International Southern Ocean Studies (ISOS,

290 Whitworth, 1983; Whitworth and Peterson, 1985). However, based on a combination of moored
291 current meter data from the DRAKE program (2006-2009) and satellite altimetry data (1992–
292 2012), Koenig et al. (2014) estimated a higher full-depth transport of 141±2.7 Sv. More recently,
293 Chidichimo et al. (2014) and Donohue et al., (2016) estimated an even higher mean ACC transport
294 of 173.3 Sv, based on the high-resolution moored bottom current and pressure measurements of
295 the cDrake program (2007-2011).

296 The modeled mean ACC transport is 157.3 Sv, about the average of the estimates from DRAKE
297 and cDrake programs. In a detailed analysis of the modeled ACC transport through the Drake
298 passage, Xu et al. (2020) found that a) the modeled ACC transport in the upper 1000 m of the
299 Drake Passage is in excellent agreement with that of Firing et al. (2011) based on shipboard
300 acoustic Doppler current profiler (SADCP) transects, and b) the modeled exponentially decaying
301 transport profile is consistent with the profile derived from the repeat hydrographic data from
302 Cunningham et al. (2003) and Meredith et al. (2011). By further comparing the model results to
303 the cDrake and DRAKE observations, Xu et al. (2020) concluded that the modeled 157.3 Sv was
304 representative of the time-mean ACC transport through Drake Passage. The cDrake experiment
305 overestimates the barotropic contribution in part because the array undersampled the deep
306 recirculation in the southern part of the Drake Passage, whereas the DRAKE experiment
307 underestimates the transport because the surface geostrophic currents yielded a weaker near-
308 surface transport than implied by the SADCP data.

309 The modeled mean zonal velocity through the Drake Passage at 65°W and the corresponding
310 volume transports for the four density layers defined earlier (surface water, AAIW, NADW,
311 AABW) are shown in Figure 11a. The ACC at this longitude exhibits four high velocity cores
312 (indicated by arrows in Figure 11a), corresponding to the ACC southern boundary (SBby, south

of 63°S), the southern ACC Front (SACCF, at 61-62°S), the Polar Front (PF, at 58-60°S), and the Sub-Antarctic Front (SAF, at 55-55°S). These modeled fronts are at similar locations as in Orsi et al. (1995) based on hydrographic surveys and in other studies based on sea surface height data (e.g., Sallée et al., 2008; Sokolov and Rintoul, 2009; Kim and Orsi, 2014).

The modeled monthly mean and 12-month moving averaged ACC transports have a standard deviation of 5.2 Sv and 2.3 Sv, respectively (Figure 12a). These numbers are relatively small compared to the long-term mean value of 157.3 Sv. The seasonal variability of the ACC transports is also small (with a standard deviation of 1.5 Sv) and exhibits a biannual pattern (Figure 13b). These results agree with the observations in Koenig et al. (2016).

3.4 Transport across the Prime Meridian-Good Hope transect

The wide ocean gap between Antarctica and the southern tip of Africa makes it difficult to fully measure the transport and its spatial structure. Observations have been collected mostly along the Prime Meridian (e.g., Whitworth and Nowlin 1987; Klatt et al. 2005) from Antarctica to approximately 50°S and the Good Hope line from 0°E, 50°S to the Cape of Good Hope, South Africa (e.g., Legeais et al., 2005; Gladyshev et al., 2008; Swart et al., 2008). We refer to the combination of these two sections as the Prime Meridian-Good Hope (PM-GH) transect (Figure 1). The modeled net transport through PM-GH (158.5 Sv) is essentially the same as the net transport through the Drake Passage because of mass conservation, except for an additional 1.2 Sv from the Pacific-to-Atlantic Bering Strait throughflow.

The modeled circulation along the PM-GH section (Figure 11b) can be divided into three regimes:

i) Weddell gyre south of 55.5°S. There are two eastward and two westward jets that form the Weddell gyre. The two westward jets are found along the Antarctic Slope and the Maud Rise (MR)

335 near 64°S, whereas the two eastward jets are found near 58-59°S and along the southern boundary
336 (SBdy) of the ACC at 55.5°S right south of the Southwest Indian Ridge (SIR). This modeled jet
337 pattern is consistent with the observations of Klatt et al., (2005, their Figures 4-5). The time mean
338 transport of the modeled Weddell gyre is 48.2 Sv, compared to 56±8 Sv estimated in Klatt et al.
339 (2005).

340 ii) ACC from 55.5°S to 40°S. The modeled ACC exhibits high-velocity cores associated with the
341 SACCF (52°S), PF (50.4°S and 48°S), SAF (44.6°S), and the subtropical front (STF, 42°S)
342 respectively. These front positions are close to the observations based on repeat CTD/XBT
343 transects in this region (Swart et al. 2008, their Table 3). Note that the PF at this location is split
344 into two fronts, with the elevated eastward velocity between 47°S and 49°S corresponding to its
345 northern expression (Swart et al. 2008; Gladyshev et al. 2008). The modeled STF is much weaker
346 than any of the other ACC fronts as in the observations. The modeled mean ACC transport across
347 the PM-GH transect, defined as the transport from 55.5°S to 40°S including the STF as in Orsi et
348 al., (1995), is 175 Sv, compared to 147-162 Sv estimated from CTD transects (Whitworth and
349 Nowlin, 1987; Legeais et al., 2005; Gladyshev et al., 2008). The modeled baroclinic transport is
350 101.2 Sv above 2500 m, compared to 84.7-97.5 Sv derived from repeated hydrographic surveys
351 and in combination with satellite altimetry data (Legeais et al., 2005; Swart et al., 2008).

352 iii) Agulhas retroflection and leakage north of 40°S. The model results show a pair of eastward
353 and westward flows associated with the Agulhas retroflection and Agulhas Current. The 'net'
354 transports north of 40°S is 9.3 and 7.9 Sv westward for the surface water and AAIW, respectively.
355 Thus, the Agulhas leakage in model provides slightly more transport than the 15.8 Sv in upper
356 AMOC.

357 The modeled transport across the full PM-GH transect decreases with depth and is eastward above
358 4000 m (blue line in Figure 13a). There is a weak westward flow below 4000 m. When compared
359 to the vertical structure of the transport in the Drake Passage (green line in Figure 13a), the
360 eastward transport through PM-GH transect is weaker in the 0-1000 m range and stronger in the
361 1000-4000 m range. This is due, in a large part, to the contributions to the northward-flowing upper
362 limb and from the southward-flowing lower limb of the AMOC (red line in Figure 13a).

363 The modeled net transports into and out of the region bounded by the 34°S, Drake Passage, and
364 PM-GH sections (see Figure1) is shown in Figure 13b. There is a net outflow above about 1400 m
365 and below 3900 m and a net inflow between these two depths. The result implies a maximum
366 upwelling transport of 5.6 Sv across 1400 m, consistent with the picture put forward by Schmitz
367 (1995) and Talley (2013) that the Southern Ocean is a key upwelling region for NADW. The net
368 transport in Figure 13b also implies a downward transport of 1.7 Sv across 3900 m, representing
369 AABW formation in the model within the region bounded by the 34°S, Drake Passage, and PM-
370 GH sections.

371 **4. Water mass transformations and circulation pathways in the South Atlantic Ocean**

372 In the previous section, we showed that the model is able to represent the basic circulation features
373 of the South Atlantic and the Southern Ocean and volume transports consistent with the
374 observations. In this section, we use the model results to address the questions raised in the
375 introduction. In subsection 4.1, we focus on the diapycnal water mass transformations associated
376 with the upwelling as shown in the previous section and, in subsection 4.2, we focus on the
377 circulation pathways of the upper and lower limbs of the AMOC.
378

379 **4.1 Diapycnal water mass transformations**

380 Similar to Figure 13b, Figure 14a shows the net transports into and out of the region bounded by
381 the 34°S, 65°W, and PM-GH sections, but with respect to density layers. The positive transports
382 (in gray bars) denote water flowing into the region (mostly NADW, but also some near surface
383 water) which is transformed and exits the region in another density class (negative transports in
384 white bars): in AABW and between the surface water and AAIW. A downward integration of these
385 layered transports gives the net transport between the sea surface and a given density surface, and
386 the difference between this integrated net transport and the change of the volume above the density
387 surface over time gives the total diapycnal water mass transformation (black line in Figure 14b)
388 taking place in the region across the given density surface; see Xu et al. (2018) for a more detailed
389 discussion on water mass transformation in the upper North Atlantic.

390 The model results in Figure 14b show significant diapycnal transformations in the region bounded
391 the 34°S, 65°W, and PM-GH sections: About 12 Sv water in the density range of 36.13-37.0 (6 Sv
392 in NADW and 6 Sv in lower AAIW) is transformed toward light water across the density surface
393 of 36.13, which means that a significant part of the AMOC closure takes place within the Atlantic
394 sector of the Southern Ocean. When compared to the transformations that are driven directly by
395 the surface buoyancy fluxes (dashed black line in Figure 14b) and calculated from the surface
396 density fluxes and surface density using the thermodynamic method (e.g., Walin 1982; Speer and
397 Tziperman, 1992; Brambilla et al., 2008; Langehaug et al., 2012; Xu et al., 2018), we find that the
398 surface-forced transformation accounts for most of the diapycnal transformation in the South
399 Atlantic region bounded by the above three sections.
400

401 **4.2 Circulation pathways of the upper and lower limb of the AMOC**

402 **a) Upper limb (surface water and AAIW)**

403 The upper (northward) limb of the AMOC consists of two density layers: the surface water
404 (σ_2<35.65) and the AAIW (35.65<σ_2<36.58 kg m^{-3}). The modeled 40-year (1979-2018) mean
405 horizontal circulation for these two layers is displayed in Figures 15 and 16, respectively. For the
406 surface water (Figure 15), the AMOC component flows directly northwestward from the Agulhas
407 Leakage into the South Atlantic (red streamlines); the subtropical gyre of the South Atlantic
408 (orange lines) flows counter-clockwise and separates the northward-flowing AMOC component
409 and the eastward-flowing ACC. There is almost no surface water in the ACC coming from the
410 Pacific Ocean (pink lines) and it does not contribute directly to the AMOC.

411 The modeled circulation pattern of the AAIW (Figure 16) is similar to the surface water (Figure
412 15), but it shows a meridionally more confined subtropical gyre (orange lines) and a larger
413 contribution to the ACC from the Pacific Ocean (pink lines). There is an indication of a 'supergyre'
414 connecting the subtropical gyres of the South Atlantic and Indian Oceans, which would further
415 prevent a direct contribution of water mass from the ACC into the upper limb of the AMOC. The
416 patterns of modeled mean circulation in Figures 15 and 16 are similar to the schematic of Stramma
417 and England (1999, their Figures 3-4), except for the recirculation in the Cape Basin which is a
418 consequence of the unrealistic pathways of the modeled Agulhas eddies (see Figures 5 and 6 and
419 discussion in subsection 3.1).

420 The model time-mean circulation in Figure 16 suggests that the Pacific AAIW does not directly
421 contribute to the upper limb of the AMOC. But this does not necessarily imply that there is no
422 contribution by the time-varying part of the circulation, e.g., eddies and meanders. To further
423 quantify the combined contribution of the mean flow and eddies by the various water mass sources,

424 we examine the water properties of the northward flow in the South Atlantic, by projecting the
425 northward transports (in Sv) on potential temperature-salinity (θ-S) plane and comparing their
426 properties with the water masses from the Pacific and the Indian Oceans (Figure 17). The Pacific
427 AAIW that flows northward across 45°S is much fresher than the Indian AAIW that flows
428 westward across the GH section (Figures 17a-b). The AAIW that flows northward across 34°S and
429 30°S is a combination of these two sources (Figures 17c-d): At 34°S, 7.8 Sv of AAIW is fresher
430 than 34.46 (Pacific) and 9.6 Sv is saltier than 34.46 (Indian). At 30°S, the Pacific contribution
431 (S<34.46) decreased to 3.6 Sv whereas the Indian contribution stayed approximately constant at
432 9.0 Sv. Further north at 25°S and 20°S (Figure 17e-f), the northward-flowing AAIW does not have
433 any distinct component of the Pacific origin, suggesting that the main contribution of the Pacific
434 AAIW in the South Atlantic is to the subtropical gyre, not to the AMOC. However, the northward-
435 flowing AAIW at 20-25°S is slightly fresher than that at GH (the transport-weighted AAIW
436 salinity is 34.56 at 20-25°S versus 34.60 at GH). This suggests that some mixing of the Indian
437 AAIW with the Pacific AAIW takes place in the South Atlantic.

438 To further study the contribution of Pacific AAIW not represented in the mean circulation (i.e.,
439 contributions by eddies), we released numerical particles into the model AAIW density layers in
440 the Drake Passage and tracked their trajectories using the modeled daily velocity fields and the
441 Lagrangian Ocean analysis toolbox OceanParcels (Delandmeter and van Sebille, 2019). The
442 particles were released across the Drake Passage at 58°W every 5 days in 1987 and 1988 and were
443 tracked for 30 years. Similar to Blanke et al. (1999), the number of particles released at each grid
444 point on the section is proportional to the model transport at that location. Each particle is tacked
445 with a small partial volume transport (<0.02 Sv) such that the cumulative volume transport of all
446 the particles reflects the instantaneous total transport for the AAIW layers through the Drake

447 Passage each time they are released. A total of 597,566 particles were released and only 36,348
448 (6.1%) of them made it north past 34°S after 30 years. This number decreases progressively as one
449 moves further north with just 12,554 (2.1%) reaching 6°S. All particles crossing 6°S are considered
450 to be part of the AMOC (e.g., Rühs et al. 2019) and Figure 18a displays the likelihood that one of
451 these particles went through a given location in the South Atlantic over the 30 years. The figure
452 shows that a) most of the particles (95%) that reached north of 6°S originated within the
453 Subantractic Front (SAF) of the ACC that is north of 56.6°S along 58°W, and b) their trajectories
454 are mostly confined to the western boundary, except for the region between 40°S and 30°S where
455 most of the particles are entrained in the interior before moving back westward.

456 The volume transport carried by all the particles that across a given latitude, divided by the number
457 of releases, provides an annual mean "Lagrangian" AAIW transport from the Drake Passage.
458 Figure 18b displays the AAIW transports across several latitudes from 34°S to 6°S as a function
459 of time. The AAIW transport across 34°S and 30°S reaches a steady state after 20-25 years at about
460 3.3 and 2.9 Sv, respectively. This transport decreases as one moves further north with only 1.0 Sv
461 across 6°S after 30 years. This transport value has not yet reached a steady state, but an exponential
462 fit using the last 15 years provides a steady state value of ~1.3 Sv. This contribution is close to the
463 latest estimate of 2 Sv by Rousselet et al. (2020) that is derived using the ECCOv4 (Estimating the
464 Circulation and Climate of the Ocean). It is, however, significantly smaller than the 4.7 Sv
465 estimated by Rühs et al. (2019) using a high-resolution ocean simulation.

466 **b) Lower limb (NADW)**

467 Figure 19 shows the modeled mean circulation for the NADW layer ($36.58<\sigma_2<37.12$). The
468 modeled NADW flows southward as a DWBC along the continental slope of the Brazil and

Argentine Basins, all the way to about 40°S where it encounters the northward-flowing deep Falkland Current. The NADW continues to flow southward (now offshore of the deep Falkland Current) to about 45°S where it meanders and flows eastward south of the Zapiola Drift (Rise). This modeled NADW pathway is similar to the one described in the schematic of Stramma and England (1999, their Figure 5) and is consistent with pathways derived from salinity, oxygen, and other tracers such as CFC (e.g., Koltermann et al., 2011; Garzoli et al., 2015). There is a strong counterclockwise flow around the Zapiola Drift (Figure 19) with a transport of approximately 25 Sv. For the full water column, the modeled long-term mean transport for this Zapiola anticyclone is about 55 Sv, consistent with the long-term mean transport of 50 Sv estimated by Saraceno et al. (2009) using observed mean dynamic topography (MDT). Higher transports have been estimated, e.g., 80 Sv by Saunders and King (1995) using on CTD/ADCP surveys and 124 Sv by Colin de Verdière and Ollitrault (2016) using Argo float data. Some of these differences may be due to the high variability in the transport on intraseasonal to interannual timescales (e.g., Saraceno et al., 2009).

South of the equator, there are complex recirculation patterns in the Brazil Basin, especially around the Vitoria-Trindade Seamount Chain near 20°S (Hogg and Owens, 1999), that carry NADW from the DWBC toward the interior of the basin and lead to high salinity all the way to the MAR in both the observations (WOCE lines A09 and A095) and the model (Figure 20). The model exhibits a zonal flow of about 2 Sv across the MAR near 22°S (Figures 19&21), which agrees with the 2 to 5 Sv estimated from observations by Warren and Speer (1991), Speer et al. (1995), Hogg and Thurnherr (2005), and Garzoli et al. (2015). East of the MAR, the modeled NADW flow turns northward and circulates around the Angola Basin as in the schematic proposed by Hogg and Thurnherr (2005). Arhan et al. (2003), however, have a much higher transport (10.7 Sv) across the

492 MAR with the NADW flowing eastward across the Angola Basin and southeastward into the Cape
493 Basin. Both the observed and modeled salinity distributions at 2500 m (Figure 20) show that
494 between 20 and 25°S, there is a large salinity difference between the east and west of the MAR
495 (A15 and A14 WOCE lines, respectively). This does not support Arhan et al. (2003)'s depiction
496 of a high-salinity NADW transport across the MAR all the way to the eastern boundary. In a
497 numerical study performed with the JAMSTEC OFES (OGCM for the Earth Simulator) model,
498 van Sebille et al. (2012) did find a continuous NADW flow east of the MAR, but the OFES model
499 also exhibited a continuous high salinity tongue (not shown here) that extends eastward across the
500 entire Angola Basin and southeastward into the Cape Basin, a result that is not supported by the
501 observations and likely an outcome of the unrealistic modeled zonal flow east of the MAR.

502 Figure 21 also shows that in NADW density range there are weak westward currents across the
503 MAR south of 22°S which lead to a lower salinity (modeled and observed) in the west basin near
504 30°S (along A10) when compared to 20-25°S (A09 and A095). Overall, there is no net transport
505 of NADW across the MAR between 20 and 40°S, thus most of the eastward NADW transport
506 occurs near 42°S where it joins the ACC water of the same density range ($36.58<\sigma_2<37.12$). The
507 NADW/ACC streamlines turn northward when approaching the MAR and southward after
508 crossing the MAR. This meridional shift can be explained by the conservation of potential
509 vorticity, f/h, i.e., a decrease in thickness h when approaching the MAR leads to a northward shift
510 to reduce the planetary rotation f so that f/h is constant and vice versa. Because the MAR is slanted
511 in a northwest-to-southeast direction in this area, the northward and southward shifts at different
512 latitude/longitude led to a contraction of the front near 10°W, which can be clearly seen in the SSH
513 for both model and observations (Figure 5).
514

5. Latitudinal coherence of the AMOC variability

The previous two sections described in detail the mean structure of the AMOC in the South Atlantic. In this section, we document its variability on seasonal to decadal time scales and address the question as to whether the AMOC variability is meridionally coherent throughout the whole Atlantic (Kelly et al., 2004; Xu et al., 2014). Using hydrography and satellite data with a box model, Kelly et al. (2014) suggested that the meridional heat transport anomalies (closely correlated with the strength of the AMOC) are highly coherent from 35°S to 40°N on interannual timescales.

The power spectral density of the modeled AMOC variability is shown in Figure 22 for ten different latitude bands between 35°S and 65°N. On timescales from one to twenty years (interannual and decadal), there is not a distinct period that the AMOC variability shows a high energy signal at all latitude bands. The power spectra distribution is similar across all latitude bands on timescales longer than 20 years, which is to be expected given that the 60-year integration is too short to truly quantify the multi-decadal variability. The only spectral peak that occurs across all latitude bands is the annual signal associated with the seasonal cycle of the atmospheric forcing. The power spectra only tell us the time scales where energy is concentrated and do not provide information on its spatial structure. In order to obtain a spatial picture of the AMOC variability on different timescales, we use the ensemble empirical mode decomposition (EEMD, Wu and Huang, 2009) to decompose the modeled AMOC transport time series (1958-2018) at individual latitudes into a number of amplitude-frequency modulated oscillatory components (termed as the intrinsic mode functions, or IMFs) successively from the highest to the lowest frequencies, without using a priori determined basis function. The advantage of the EEMD method is that both the frequency and amplitude of each IMF are determined adaptively from the local characteristic of the time

538 series and they vary as a function of time. The same IMF at all latitudes (here from 35°S to 70°N
539 with 0.5° resolution) can be pieced together to construct the basin-scale pattern of the AMOC
540 variability.

541 There are total of nine IMFs for the 60-year monthly mean time series (the first two IMFs represent
542 the high-frequency intraseasonal variability). The third IMF (Figure 23) represents the variability
543 of the AMOC transport on seasonal timescale. The results show that the seasonal AMOC
544 variability is high at all latitudes (Figure 22). It appears at a first glance that the variability is quite
545 coherent across all latitudes, but there is actually a phase shift that occurs around 15°N. This is
546 illustrated by the right panel of Figure 23 that displays the mean seasonal variability. The phase in
547 the subtropical North Atlantic is constant from 15 to 45°N and lags the variability further north in
548 subpolar North Atlantic. South of 15°N, the phase in the equatorial region leads that of the South
549 Atlantic Ocean. This phase shift can be seen in observations as well. For example, high seasonal
550 AMOC transports occur during April-August at 34°S (Figure 10b based on Argo-WOA13 data),
551 compared to July-November at 26.5°N (Figure 4c based on RAPID data). Most of the AMOC
552 seasonal variability as well as the phase shift is due to variability in the wind-driven Ekman
553 transport as discussed by Xu et al. (2014), Zhao and Johns (2014a), and Yang (2015).

554 The fourth and fifth IMFs displayed in Figure 24 represent the interannual variability. Its
555 magnitude is smaller than that of the seasonal variability, but the phases are relatively constant
556 across a wide latitudinal range. In order to quantitatively measure the meridional coherence, we
557 compute the correlation between the interannual variability at a given latitude and the variability
558 averaged through the whole Atlantic from 35°S to 70°N (see Xu et al., 2019 for an example). The
559 correlation, shown in Figure 25, is significant from 35°S to 35°N. This result is in good agreement

with the findings of Kelly et al. (2014) based on observations and box model, except that their correlation extends further north to 40°N. As for the seasonal time scale, the interannual variability of the AMOC is primarily driven by the wind variability (e.g., Roberts et al., 2013; Zhao and Johns, 2014b).

Figure 26 shows the sixth IMF and the sum of the seventh to ninth IMFs, representing the AMOC variability on decadal and multi-decadal timescales, respectively. The 60-year simulation is too short to allow for a robust quantification of the multi-decadal variabilities (Figure 26b), but we find that the variability is consistent with century-long ocean-only simulations performed with CORE-II (Danabasoglu et al., 2016; Xu et al., 2019). The decadal variability (Figure 26a) is mostly coherent south of 35°N, as for the interannual variability shown in Figure 25. North of 35°N, there is sometimes a phase shift with variability of the subpolar North Atlantic leading the variability further south. This aspect of the decadal variability (i.e., with origin in the subpolar North Atlantic near 50°N and propagating southward) has been reported previously in several basin scale simulations (Böning et al. 2006; Xu et al., 2013).

6. Summary and Discussion

Through the South Atlantic Ocean, the AMOC is connected to the Indian/Pacific Oceans and is entangled into the global overturning circulation system. This important region is also particularly complex, featuring strong boundary currents (jets) and high eddy variability in both the western and eastern boundaries as well as in the Atlantic sector of the Southern Ocean. Observations of the full-depth circulation structure are focused on limited places, thus the three-dimensional circulation structure in the South Atlantic and the large-scale pattern of the AMOC variability are not well-determined. In this study, we used numerical results from a long-term 1/12° global simulation, along with observations, to address the fundamental questions regarding the mean

583 circulation pattern in this region as well as the meridional coherence of the AMOC variability. The
584 model results are shown to represent the transports and the vertical structure of the key circulation
585 patterns in this region, especially, the AMOC across 34°S in the South Atlantic, the ACC at 65°W
586 in the Drake Passage, as well as the zonal flows along the PM-GH transect in the open ocean
587 southwest of Africa. The key results are:

588 1) In the South Atlantic Ocean south of 34°S between the Drake Passage (65°W) and southwest
589 of Africa (PM-GH), there is a maximum upward transport of 5.6 Sv across 1400 m. The water in
590 this area undergoes a strong diapycnal transformation: about 12 Sv AAIW and NADW in the
591 density range of 36.13-37.0 kg/m^3 is transformed toward lighter intermediate water, mostly due to
592 surface buoyancy forcing.

593 2) In the upper limb of the AMOC, the northward flow originates primarily from the warm Agulhas
594 leakage. The colder fresher Pacific water also enters the South Atlantic Ocean via eddy motions.
595 The cold water participates the subtropical gyre and modifies the water properties of the South
596 Atlantic Ocean; its direct contribution to the northward limb of the AMOC is relatively small (in
597 the order of 1.5 Sv).

598 3) In the lower limb, the NADW flows southward in the DWBC along the continental slope and
599 in complex recirculation in the Brazil Basin, especially around the Vitória-Trindade Seamount
600 Chain near 20°S. The recirculation carries the NADW and its high-salinity signature into the
601 offshore interior. A weak zonal flow of NADW of ~2 Sv is found to cross the MAR near 22°S.
602 Different from the schematic of Arhan et al. (2003) based on inverse model and the previous
603 numerical results of van Sebille et al. (2012), however, this modeled NADW does not continue to
604 flow eastward across the Angola Basin and southeastward into the Cape Basin. Instead, it turns
605 northward and circulates around the Angola Basin like the schematic proposed by Hogg and

606 Thurnherr (2005). This NADW circulation pattern is consistent with the water property
607 distribution, i.e., in both observations and model, the salinity east of MAR is significantly lower
608 than that to the west. Virtually all of the NADW from the north flows in the DWBC all the way to
609 40-45°S before turning eastward to flow across the MAR near 42°S. The location of this crossing
610 can be seen from SSH as a contracted ACC front near 10°W.

611 4) Overall, the modeled AMOC variability from interannual to decadal timescales is meridional
612 coherent in the Atlantic Ocean from 35°S to about 35°N, in agreement with Kelly et al. (2014).
613 One may expect a higher degree of meridional coherence in this latitude range because, being
614 outside of the deep-water formation and/or the upwelling regions, the diapycnal water mass
615 transformation between the upper and lower AMOC limbs is small and the variability is mostly
616 wind driven.

617 Although the modeled transport and vertical structure of the South Atlantic presented in this study
618 are largely consistent with the observations, there is room for improvement. In particular, the
619 modeled Agulhas rings dissipate too slowly and follow a regular pathway. This leads to a high
620 EKE tongue that extends much farther to the northwest and impacts the regional circulation pattern
621 in the eastern South Atlantic. Several remedies have been put forward to improve the realism of
622 the circulation in the Agulhas region, namely i) using finer horizontal resolution along with a better
623 representation of the bathymetry features like the Agulhas Bank/Plateau as well as the continental
624 slope and seamounts (Speich et al., 2006); ii) using a higher order advection scheme which would
625 lead to more irregularity in Agulhas eddy size and pathway (Backeberg et al., 2009), or iii)
626 including the ocean current feedback in the wind stress calculation (Renault et al., 2017;
627 Chassignet et al., 2020). While it is indeed more physical to take into account the vertical shear
628 between atmospheric winds and ocean currents when computing the wind stress, it does lead to an

eddy damping effect that can reduce the kinetic energy by as much as 30% and lead to a serious underestimation of EKE elsewhere in the domain (Chassignet et al., 2020). There is therefore a trade-off between a better representation of one current system (the Agulhas) and realistic energetic and/or variability throughout the globe.

Acknowledgement: The work is supported by NOAA-Earth System Prediction Capability Project (Award NA15OAR4320064), NOAA Climate Program Office MAPP Program (Award NA15OAR4310088), and Climate Variability and Predictability Program (Award GC16-210), and NOAA's Atlantic Oceanographic and Meteorological Laboratory. The numerical simulations were performed on supercomputers at the Engineer Research and Development Center (ERDC), Vicksburg, Mississippi, using computer time provided by the U.S. DoD High Performance Computing Modernization Program. The sea ice extent data are available from National Snow & Ice data Center (https://nsidc.org/data); the altimeter products used here were produced by Ssalto/Duacs and distributed AVISO, with support from CNES http://www.aviso.altimetry.fr/duacs; the gridded T/S fields from the Argo float measurements are available at http://www.argo.ucsd.edu/Gridded_fields.html and the World Ocean Atlas 2013 is available at http://www.nodc.noaa.gov/OC5/woa13; the velocity at 1000 m is obtained from http://apdrc.soest.hawaii.edu/projects/Argo/data/trjctry; the global model outputs are stored in the ERDC archive server and the model results presented in this study are available in HYCOM server (ftp://ftp.hycom.org/pub/xbxu/GLBb0.08/SATL).

Reference:

Arhan, M., Mercier H., & Park Y.-H. (2003). On the deep water circulation of the eastern South Atlantic Ocean. *Deep-Sea Research Part I*, **50**, 889–916, https://doi.org/10.1016/S0967-0637(03)00072-4

Backeberg, B. C., Bertino, L., & Johannessen, J. A. (2009). Evaluating two numerical advection schemes in HYCOM for eddy-resolving modelling of the Agulhas Current, *Ocean Science*, **5**, 173-190, https://doi.org/10.5194/os-5-173-2009

Baringer, O. M., & Garzoli, S. L. (2007). Meridional heat transport determined with expendable bathythermographs. Part I: Error estimates from model and hydrographic data. *Deep-Sea Research Part I*, **54**, 1390–1401, https://doi.org/10.1016/j.dsr.2007.03.011

Beal, L. M., De Ruijter, W. P. M., Biastoch, A., Zahn, R., & SCOR/WCRP/IAPSO Working Group 136 (2011). On the role of the Agulhas system in ocean circulation and climate, *Nature*, **472** (7344), 429–436, https://doi.org/10.1038/nature09983

Bleck, R. (2002). An oceanic general circulation model framed in hybrid isopycnic-Cartesian coordinates. *Ocean Modelling*, **37**, 55–88.

Böning, C. W., Scheinert, M., Dengg, J., Biastoch, A., & Funk, A. (2006). Decadal variability of subpolar gyre transport and its reverberation in the North Atlantic overturning, Geophys. Res. Lett., **33**, L21S01, https://doi.org/10.1029/2006GL026906.

Bower, A., Lozier, S., Biastoch, A., Drouin, K., Foukal, N., Furey, H., et al. (2019). Lagrangian views of the pathways of the Atlantic Meridional Overturning Circulation. *Journal of Geophysical Research: Oceans*, **124** (8), 5313-5335. https://doi.org/10.1029/2019JC015014

Brambilla, E., Talley, L. D. & Robbins, P. E. (2008). Subpolar Mode Water in the northeastern Atlantic: 2. Origin and transformation. *Journal of Geophysical Research: Oceans*, **113**(C4). https://doi.org/10.1029/2006JC004063

Broeker, W. S. (1991). The great ocean conveyor, *Oceanography*, **4** (2):79–89.

Carnes, M. R. (2009). Description and evaluation of GDEM-V3.0. Tech. Rep. NRL/MR/7330–09–9165, 21 pp., Naval Research Laboratory, Stennis Space Center, Miss.

Chassignet, E. P., Smith, L. T., Halliwell, G. R. & Bleck, R. (2003). North Atlantic simulations with the hybrid coordinate ocean model (HYCOM): Impact of the vertical coordinate choice, reference pressure, and thermobaricity, *Journal of Physical Oceanography*, **33** (12), 2504–2526.

Chassignet, E. P., Hurlburt, H. E., Smedstad, O. M., Halliwell, G. R., Wallcraft, A. J., Metzger, E. J., et al. (2006). Generalized vertical coordinates for eddy-resolving global and coastal ocean forecasts, *Oceanography*, **19** (1), 20–31. https://doi.org/10.5670/oceanog.2006.95

Chassignet, E. P., Yeager, S. G., Fox-Kemper, B., Bozec, A., Castruccio, F., Danabasoglu, G. et al. (2020). Impact of horizontal resolution on global ocean-sea-ice model simulations based on the experimental protocols of the Ocean Model Intercomparison Project phase 2 (OMIP-2), *Geoscientific Model Development*, https://doi.org/10.5194/gmd-2019-374-RC2

Chidichimo, M. P., Donohue, K. A., Watts, D. R., & Tracey, K. L. (2014). Baroclinic transport time series of the Antarctic Circumpolar Current measured in Drake Passage, *Journal of Physical Oceanography*, **44** (7), 1829–1853. https://doi.org/10.1175/JPO-D-13-071.1

Colin de Verdière, A., & Ollitrault, M. (2016). A direct determination of the World Ocean barotropic circulation, Journal of Physical Oceanography, 46, 255-273, https://doi.org/10.1175/JPO-D-15-0046.1.

Cunningham, S. A., Alderson, S. G., King, B. A., & Brandon M. A. (2003). Transport and variability of the Antarctic Circumpolar Current in Drake Passage, *Journal of Geophysical Research-Oceans*, **108** (C5), 8084, https://doi.org/10.1029/2001JC001147.

694 Delandmeter, P., & van Sebille, E. (2019). The Parcels v2.0 Lagrangian framework: new field interpolation
695 schemes, *Geoscientific Model Development*, **12**, 3571–3584, https://doi.org/10.5194/gmd-12-3571-
696 2019.
697 Dong, S., Garzoli, S., Baringer, M., Meinen, C., & Goni, G. (2009). Interannual variations in the Atlantic
698 meridional overturning circulation and its relationship with the net northward heat transport in the South
699 Atlantic. *Geophysical Research Letter*, **36**, L20606, https://doi.org/10.1029/2009GL039356.
700 Dong, S., Garzoli, S., & Baringer, M. (2011). The Role of inter-ocean exchanges on decadal variations of
701 the meridional heat transport in the South Atlantic. *Journal of Physical Oceanography*, **41**, 1498–1511.
702 https://doi.org/ 10.1175/2011JPO4549.1.
703 Dong, S., Baringer, M. O., Goni, G. J. Meinen, C. S., & Garzoli, S. L. (2014). Seasonal variations in the
704 South Atlantic meridional overturning circulation from observations and numerical models,
705 *Geophysical Research Letter*, **41**, 4611–4618, https://doi.org/10.1002/2014GL060428.
706 Dong, S., Goni, G., & Bringas, F. (2015). Temporal variability of the South Atlantic Meridional
707 Overturning Circulation between 20°S and 35°S, *Geophysical Research Letter*, **42**, 7655–7662,
708 https://doi.org/10.1002/2015GL065603.
709 Donners, J., & Drijfhout, S. S. (2004). The Lagrangian view of South Atlantic interocean exchange in a
710 global ocean model compared with inverse model results, *Journal of Physical Oceanography*, **34** (5),
711 1019–1035.
712 Donohue, K. A., Tracey, K. L., Watts, D. R., Chidichimo, M. P., & Chereskin, T. K. (2016). Mean Antarctic
713 Circumpolar Current transport measured in Drake Passage. *Geophysical Research Letters*, **43**, 11760–
714 11767. https://doi.org/10.1002/2016GL070319.
715 Fetterer, F., Knowles, K., Meier, W., Savoie, M., & Windnagel. A. K. (2017). Sea Ice Index, Version 3.
716 Boulder, Colorado USA. NSIDC: National Snow and Ice Data Center.
717 http://dx.doi.org/10.7265/N5K072F8.
718 Firing, Y. L., Chereskin, T. K., & Mazloff, M. R. (2011). Vertical structure and transport of the Antarctic
719 Circumpolar Current in Drake Passage from direct velocity observations, *Journal of Geophysical*
720 *Research-Oceans*, **116**, https://doi.org/10.1029/2011JC006999.
721 Friocourt, Y., Drijfhout, S., Blanke, B., & Speich, S. (2005). Water mass export from Drake Passage to the
722 Atlantic, Indian, and Pacific Oceans: A Lagrangian model analysis. *Journal of Physical Oceanography*,
723 **35** (7), 1206–1222. https://doi.org/10.1175/JPO2748.1
724 Garzoli, S. L., & Matano, R. (2011). The South Atlantic and the Atlantic Meridional Overturning
725 Circulation, *Deep-Sea Research Part II*, **58** (17-18), 1837–1847,
726 https://doi.org/10.1016/j.dsr2.2010.10.063.
727 Garzoli, S. L., Baringer, M. O., Dong, S., Perez, R. C., & Yao, Q. (2013). South Atlantic meridional fluxes,
728 *Deep-Sea Research Part I*, **71**, 21–32, https://doi.org/10.1016/j.dsr.2012.09.003.
729 Garzoli, S. L., Dong, S., Fine, R., Meinen, C. S., Perez, R. C., Schmid, C., et al. (2015). The fate of the
730 Deep Western Boundary Current in the South Atlantic, *Deep-Sea Research Part I*, **103**, 125–136,
731 https://doi.org/10.1016/j.dsr.2015.05.008.
732 Gladyshev, S., Arhan, M., Sokov, A., & Speich S. (2008). A hydrographic section from South Africa to
733 the southern limit of the Antarctic Circumpolar Current at the Greenwich meridian, *Deep-Sea Research*
734 *Part I*, **55**, 1284–1303, https://doi.org/10.1016/j.dsr.2008.05.009.
735 Goes, M., Goni, G. & Dong, S. (2015). An optimal XBT-based monitoring system for the South Atlantic
736 meridional overturning circulation at 34S, *Journal of Geophysical Research-Oceans*, **120**, 161–181,
737 https://doi.org/10.1002/2014JC010202.

738 Gordon, A. L. (1986). Interocean exchange of thermocline water, *Journal of Geophysical Research-*
739 *Oceans*, **91** (C4), 5037–5046, https://doi.org/10.1029/JC091iC04p05037.
740 Gordon, A.L. (2001). Interocean Exchange. in *Ocean Circulation and Climate*, G. Siedler, J. Church, and
741 J. Gould, eds. Academic Press. Chapter 4.7, 303–314.
742 Hogg, N. G., & Owens, W. B. (1999). Direct measurement of the deep circulation within the Brazil Basin.
743 *Deep-Sea Research Part II.* **46**, 335–353, http://dx.doi.org/10.1029/2004/JC002311.
744 Hogg, N. G., & Thurnherr, A. M. (2005). A zonal pathway for NADW in the South Atlantic. *Journal of*
745 *Oceanography*. **61**(3), 493–507, https://doi.org/10.1007/s10872-005-0058-7.
746 Hogg, N. G., Biscaye, P. E., Gardner, W. D., & Schmitz, W. J. Jr. (1982). On the Transport and Modification
747 of Antarctic Bottom Water in the Vema Channel, *Journal of Marine Research*, **40**, 231-263.
748 Hunke, E. C., & Lipscomb, W. H. (2008). CICE: The Los Alamos sea ice model documentation and
749 software user's manual, version 4.0, Tech. Rep. LA-CC-06-012, Los Alamos Natl. Lab., Los Alamos,
750 N. M.
751 Kelly, K. A., Thompson, L., & Lyman, J. (2014). The coherence and impact of meridional heat transport
752 anomalies in the Atlantic Ocean inferred from observations, *Journal of Climate*, **27**, 1469–1487,
753 https://doi.org/10.1175/JCLI-D-12-00131.1.
754 Kim, Y. S., & Orsi, A. H. (2014). On the variability of Antarctic Circumpolar Current fronts inferred from
755 1992–2011 altimetry, *Journal of Physical Oceanography*, **44** (12), 3054–3071,
756 https://doi.org/10.1175/JPO-D-13-0217.1.
757 Klatt, O., Fahrbach, E., Hoppeman, M. & Rohardt, G. (2005). The transport of the Weddell Gyre across the
758 prime meridian, *Deep-Sea Research Part II*, **52**, 513–528. https://doi.org/10.1016/j.dsr2.2004.12.015.
759 Kersalé, M., Perez, R. C., Speich, S., Meinen, C. S., Lamont, T., Le Hénaff, M., et al. (2019). Shallow and
760 Deep Eastern Boundary Currents in the South Atlantic at 34.5°S: Mean structure and variability, *Journal*
761 *of Geophysical Research-Oceans*, https://doi.ogr/10.1029/2018JC014554.
762 Koenig Z., Provost, C., Ferrari, R., Sennéchael, N., & Rio, M.-H. (2014). Volume transport of the Antarctic
763 Circumpolar Current: Production and validation of a 20 year long times series obtained from in situ and
764 satellite data, *Journal of Geophysical Research-Oceans*, **119**, 5407–5433,
765 https://doi.org/10.1002/2014JC009966.
766 Koenig, Z., Provost, C., Park, Y.-H., Ferrari, R., & Sennéchael, N. (2016). Anatomy of the Antarctic
767 Circumpolar Current volume transports through Drake Passage, *Journal of Geophysical Research-*
768 *Oceans*, **121**, 2572–2595, https://doi.org/10.1002/2015JC011436.
769 Koltermann, K.P., Gouretski, V.V. & Jancke, K. (2011). Hydrographic Atlas of the World Ocean
770 Circulation Experiment (WOCE). Volume 3: Atlantic Ocean (eds. M. Sparrow, P. Chapman and J.
771 Gould). International WOCE Project Office, Southampton, UK, ISBN 090417557X.
772 Langehaug, H. R., Rhines, P. B., Eldevik, T., Mignot, J., & Lohmann, K. (2012). Water mass transformation
773 and the North Atlantic Current in three multicentury climate model simulations. *Journal of Geophysical*
774 *Research-Oceans*, **117** (C11), https://doi.org/10.1029/2012JC008021.
775 Large, W. G., & Yeager, S. (2004). Diurnal to decadal global forcing for ocean and sea-ice models: The
776 data sets and flux climatologies. NCAR Tech. Note NCAR/TN 460+STR.
777 Legeais, J. F., Speich, S., Arhan, M., Ansorge, I. J., Fahrbach, E., Garzoli, S., & Klepikov, A. (2005). The
778 baroclinic transport of the Antarctic Circumpolar Current south of Africa, *Geophysical Research Letter*,
779 **32**, L24602, https://doi.org/10.1029/2005GL023271.

780 Locarnini, R. A., Mishonov, A. V., Antonov, J. I., Boyer, T. P., Garcia, H. E., Baranova, O. K., et al. (2013).
781 Temperature. Vol. 1, World Ocean Atlas 2013, S. Levitus, Ed., A. Mishonov Technical Ed., NOAA
782 Atlas NESDIS 73, 40 pp.
783 Loeb, N. G., Lyman, J. M., Johnson, G. C. Allan, R. P., Doelling, D. R., Wong, T., et al. (2012). Observed
784 changes in top-of-the-atmosphere radiation and upper-ocean heating consistent within uncertainty,
785 *Nature Geoscience*, **5**, 110–113, doi:10.1038/NGEO1375.
786 Macdonald, A. M., & Baringer, M. O. (2013). Ocean heat transport. In *Ocean Circulation and Climate: A*
787 *21st Century Perspective*, G. Siedler et al., Eds., International Geophysics Series, **103**, Academic Press,
788 759–786, https://doi.org/10.1016/ B978-0-12-391851-2.00029-5.
789 Maltrud, E.M., & McClean, J. (2005). An Eddy Resolving Global 1/10º Ocean Simulation, *Ocean*
790 *Modelling*, **8**, 31-54, http://dx.doi.org/10.1016/j.ocemod.2003.12.001.
791 Meinen, C. S., Piola, A. R., Perez, R. C., & Garzoli, S. L. (2012). Deep Western Boundary Current transport
792 variability in the South Atlantic: preliminary results from a pilot array at 34.5ºS, *Ocean Science*, **8**,
793 1041–1054, https://doi.org/10.5194/os-8-1041-2012.
794 Meinen, C. S., Speich, S., Perez, R. C., Dong, S., Piola, A. R., Garzoli, S. L., et al. (2013). Temporal
795 variability of the Meridional Overturning Circulation at 34.5ºS: Results from two pilot boundary arrays
796 in the South Atlantic, *Journal of Geophysical Research-Oceans*, **118**, 6461–6478,
797 https://doi.org/10.1002/2013JC009228.
798 Meinen, C. S., Garzoli, S. L., Perez, R. C., Campos, E., Piola, A. R., Chidichimo, M. P., et al. (2017).
799 Characteristics and causes of Deep Western Boundary Current transport variability at 34.5ºS during
800 2009–2014, *Ocean Science*, **13**, 175-194, https://doi.org/10.5194/os-13-175-2017.
801 Meinen, C. S., Speich, S., Piola, A. R., Ansorge, I., Campos, E., Kersalé, M., et al. (2018). Meridional
802 Overturning Circulation transport variability at 34.5ºS during 2009–2017: Baroclinic and barotropic
803 flows and the dueling influence of the boundaries, *Geophysical Research Letter*, **45**, 4180–4188,
804 https://doi.org/10.1029/2018GL077408.
805 Meredith, M. P., Woodworth, P. L., Chereskin, T. K., Marshall, D. P., Allison, L. C., Bigg, G. R., et al.
806 (2011). Sustained monitoring of the Southern Ocean at Drake Passage: Past achievements and future
807 priorities. *Reviews of Geophysics*, **49**, RG4005. https://doi.org/10.1029/2010RG000348.
808 Mulet, S., Rio, M. H., Etienne, H., Artana, C., Cancet, M., Dibarboure, G., et al. (2020). The new CNES-
809 CLS18 Global Mean Dynamic Topography, Submitted to *Ocean Science*.
810 Orsi, A. H., Whitworth, T. III, & Nowlin, W. D. Jr. (1995). On the meridional extent and fronts of the
811 Antarctic Circumpolar Current, *Deep-Sea Research Part I*, **42**, 641–673.
812 Renault, L., McWilliams, J. C., & Penven, P. (2017). Modulation of the Agulhas Current retroflection and
813 leakage by oceanic current interaction with the atmosphere in coupled simulations, *Journal Physical*
814 *Oceanography*, 47, 2077–2100, https://doi.org/10.1175/JPOD-16-0168.1.
815 Richardson, P. L. (2007). Agulhas leakage into the Atlantic estimated with subsurface floats and surface
816 drifters, *Deep-Sea Research Part I*, **54**, 1361–1389, https://doi.org/10.1016/j.dsr.2007.04.010.
817 Richardson, P. L. (2008). On the history of meridional overturning circulation schematic diagrams.
818 *Progress in Oceanography*, **76**, 466-486, https://doi.org/10.1016/j.pocean.2008.01.005.
819 Rintoul, S. R. (1991). South Atlantic interbasin exchange, *Journal of Geophysical Research-Oceans*, **96**
820 (C2), 2675–2692, https://doi.org/10.1029/90JC02422.
821 Roberts, C. D., Waters, J., Peterson, K. A., Palmer, M. D., McCarthy, G. D., Frajka-Williams, E., et al.
822 (2013). Atmosphere drives recent interannual variability of the Atlantic meridional overturning
823 circulation at 26.5°N, *Geophysical Research Letters*, **40**, 5164–5170, https://doi.org/10.1002/grl.50930.

Roemmich, D., Church, J., Gilson, J., Monselesan, D., Sutton, P., & Wijffels, S. (2015). Unabated planetary warming and its ocean structure since 2006. *Nature Climate Change*. **5**, 240-245, https://doi.org/10.1038/nclimate2514.

Rodrigues, R. R., Wimbush, M., Watts, D. R., Rothstein, L. M., & Ollitrault, M. (2010). South Atlantic mass transports obtained from subsurface float and hydrographic data. *Journal of Marine Research*, **68**, 819– 850, https://doi.org/10.1357/002224010796673858.

Rousselet, L., Cessi, P., & Forget, G. (2020). Routes of the upper branch of the Atlantic meridional overturning circulation according to an ocean state estimate, *Geophyical Research Letters*, https://doi.org/10.1029/2020GL089137.

Rühs, S., Schwarzkopf, F. U., Speich, S., & Biastoch, A. (2019). Cold vs. warm water route—Sources for the upper limb of the Atlantic meridional overturning circulation revisited in a high-resolution ocean model, *Ocean Science*, **15**, 489–512.

Sallée, J.-B., Speer, K., & Morrow, R. (2008). Response of the Antarctic Circumpolar Current to atmospheric variability, *Journal of Climate*, **21** (12), 3020–30391, https://doi.org/10.1175/2007JCLI1702.1.

Saracerno, M., Provost, C., & Zajaczkovski, U. (2009). Long-term variation in the anticyclonic ocean circulation over Zapiola Rise as observed by satellite altimetry: Evidence of possible collapses, *Deep-Sea Research Part I*, 56, 1077-1092, https://doi.org/10.1016/j.dsr.2009.03.005.

Saunders, P. M., & King, B. A. (1995). Oceanic fluxes on the WOCE A11 section, *Journal of Physical Oceanography*, **25**, 1942–1958.

Schlitzer, R. (1996). Mass and Heat Transports in the South Atlantic Derived from Historical Hydrographie Data, in *The South Atlantic*. Springer, Berlin, Heidelberg

Schmitz, W. J. Jr. (1995). On the interbasin-scale thermohaline circulation, *Reviews of Geophysics*, **33** (2), 151–173, https://doi.org/10.1029/95RG00879.

Schmitz, W. J. Jr. (1996). On the World Ocean Circulation: Volume I. Technical Report, WHOI-96-03. 140 pp.

Smeed, D. A., Josey, S. A., Beaulieu, C., Johns, W. E., Moat, B. I., Frajka-Williams, E., et al. (2018). The North Atlantic Ocean is in a state of reduced overturning, *Geophysical Research Letters*, **45**, 1527–1533, https://doi.org/10.1002/ 2017GL076350.

Sokolov, S., & Rintoul, S. R. (2009). Circumpolar structure and distribution of the Antarctic Circumpolar Current fronts: 1. Mean circumpolar paths, *Journal of Geophysical Research*, **114**, C11018, https://doi.org/10.1029/2008JC005108.

Speer, K. & Tziperman, E. (1992). Rates of water mass formation in the North Atlantic Ocean, *Journal of Physical Oceanography*, **22**(1), 93-104.

Speer, K. G., Siedler, G. & Talley, L. (1995). The Namib Col Current, *Deep-Sea Research Part I*, **42**, 1933–1950.

Speer, K. G. & Zenk, W. (1993). The flow of Antarctic Bottom Water into the Brazil Basin, *Journal of Physical Oceanography*, **23**, 2667-2682.

Speich, S., Blanke, B., & Madec, G. (2001). Warm and cold water routes of an OGCM thermohaline conveyor belt, *Geophysical Research Letters*, **28**, 311–314.

Speich, S., Lutjeharms, J. R. E., Penven, P., & Blanke, B. (2006). Role of bathymetry in Agulhas Current configuration and behaviour, Geophysical Research Letters., **33**, L23611, doi:10.1029/2006GL027157.

Stramma, L., & England, M. (1999). On the water masses and mean circulation of the South Atlantic Ocean, *Journal of Geophysical Research*, **104**, 20,863–20,883, https://doi.org/10.1029/1999JC900139.

868 Swart, S., Speich, S., Ansorge, I. J., Goni, G. J., Gladyshev, S. & Lutjeharms, J. R. E. (2008). Transport
869 and variability of the Antarctic Circumpolar Current south of Africa, *Journal of Geophysical Research-*
870 *Oceans*, **113**, C09014, https://doi.org/10.1029/2007JC004223.
871 Talley, L. D. (2013). Closure of the Global Overturning Circulation Through the Indian, Pacific, and
872 Southern Oceans: Schematics and Transports. *Oceanography*, **26** (1), 80–97,
873 https://doi.org/10.5670/oceanog.2013.07.
874 Trenberth, K. E., Zhang, Y., Fasullo, J. T. & Cheng, L. (2019). Observation-based estimates of global and
875 basin ocean meridional heat transport time series, *Journal of Climate*, 4567-4583,
876 https://doi.org/10.1175/JCLI-D-18-0872.1.
877 Tsujino H., Urakawa, S., Nakano, H., Small, R. J., Kim, W. M., Yeager, S. G. et al. (2018). JRA-55 based
878 surface dataset for driving ocean-sea-ice models (JRA55-do), *Ocean Modelling*, **130**, 79-139,
879 https://doi.org/10.1016/j.ocemod.2018.07.002.
880 van Sebille, E., Johns, W. E., & Beal, L. M. (2012). Does the vorticity flux from Agulhas rings control the
881 zonalpathway of NADW across the South Atlantic? *Journal of Geophysical Research: Oceans*, **117**,
882 C05037, https://doi.org/10.1029/2011JC007684.
883 Walin, G. (1982). On the relation between sea-surface heat flow and thermal circulation in the ocean,
884 *Tellus*, **34** (2), 187-195.
885 Warren, B. A. & Speer, K. G. (1991). Deep circulation in the eastern South Atlantic Ocean, *Deep-Sea*
886 *Research Part I*, **38** (1991), S281-S322.
887 Whitworth, T. III (1983). Monitoring the transport of the Antarctic Circumpolar Current at Drake Passage,
888 *Journal of Physical Oceanography*, **13**, 2045–2057.
889 Whitworth, T., III, & Peterson R. G. (1985). Volume transport of the Antarctic Circumpolar Current from
890 bottom pressure measurements, *Journal of Physical Oceanography*, **15**, 810–816.
891 Whitworth, T., & Nowlin, W. D. (1987). Water masses and currents of the Southern Ocean at the
892 Greenwich meridian, *Journal of Geophysical Research*, **92** (C6), 6462– 6476.
893 Wu, Z., & Huang, N. E. (2009). Ensemble empirical mode decomposition: A noise-assisted data analysis
894 method, *Advances in Adaptive Data Analysis*, **1** (1), 1–41, https://doi.org/10.1142/S1793536909000047
895 Xu, X., Hurlburt, H. E., Schmitz, W. J. Jr., Fischer, J., Zantopp, R., & Hogan, P. J. (2013). On the currents
896 and transports connected with the Atlantic meridional overturning circulation in the subpolar North
897 Atlantic, *Journal of Geophysical Research: Oceans*, **118**, doi:10.1002/jgrc.20065.
898 Xu, X., Chassignet, E. P., Johns, W. E., Schmitz W. J. Jr., & Metzger, E. J. (2014). Intraseasonal to
899 interannual variability of the Atlantic meridional overturning circulation from eddy-resolving
900 simulations and observations. *Journal of Geophysical Research: Oceans*, **119**, 5140–5159,
901 https://doi.org/10.1002/2014JC009994.
902 Xu, X., Rhines, P. B., & Chassignet, E. P. (2018). On mapping the diapycnal water mass transformation of
903 the upper North Atlantic Ocean, *Journal of Physical Oceanography*, **48**, 2233-2258,
904 https://doi.org/10.1175/JPO-D-17-0223.1.
905 Xu, X., Chassignet, E. P., & Wang, F. (2019). On the variability of the Atlantic meridional overturning
906 circulation transports in coupled CMIP5 simulations, *Climate Dynamics*,
907 https://doi.org/10.1007/s00382-018-4529-0.
908 Xu, X., Chassignet, E. P., Firing, Y. L., & Donohue, K. (2020). Antarctic Circumpolar Current transport
909 through Drake Passage: What can we learn from comparing high-resolution model results to
910 observations? *Journal of Geophysical Research: Oceans*, **125**, e2020JC016365,
911 https://doi.org/10.1029/2020JC016365.

912 Yang, J. (2015). Local and remote wind-stress forcing of the seasonal variability of the Atlantic Meridional
913 Overturning Circulation (AMOC) transport at 26.5ºN. *Journal of Geophysical Research: Oceans*, **120**,
914 doi:10.1002/2014JC010317.
915 Zhang, R. (2010). Latitudinal dependence of Atlantic meridional overturning circulation (AMOC)
916 variations, *Geophysical Research Letter*, **37**, L16703, https://doi.org/10.1029/2010GL044474.
917 Zhao, J., & Johns, W. E. (2014a). Wind driven seasonal cycle of the Atlantic meridional overturning
918 circulation, *Journal of Physical Oceanography*, **44** (6), 1541–1562, doi:10.1175/JPO-D-13-0144.1.
919 Zhao, J., & Johns, W. E. (2014b). Wind-forced interannual variability of the Atlantic meridional
920 overturning circulation at 26.5ºN, *Journal of Geophysical Research: Oceans*, **119**, 2403–2419,
921 doi:10.1002/2013JC009407.
922 Zweng, M. M., Reagan, J. R., Antonov, J. I., Locarnini, R. A., Mishonov, A.V., Boyer, T.P., et al. (2013).
923 Salinity. Vol. 2, World Ocean Atlas 2013, S. Levitus, Ed., A. Mishonov Technical Ed.; NOAA Atlas
924 NESDIS 74, 39 pp.
925

Figure Caption

Figure 1: Model bathymetry (in km) along with key topographic features in the South Atlantic Ocean. Red lines denote three sections where significant observations have been obtained and the observations are used to evaluate the model results: 34°S in the South Atlantic, 65°W in Drake Passage, and the Prime Meridian-Good Hope (PM-GH) transect southwest of Africa.

Figure 2: Time evolution of global domain-averaged a) potential temperature in °C and b) total kinetic energy in cm^2s^{-2} from the global ocean-sea ice simulation. Thin and thick lines denote monthly and annual means, respectively.

Figure 3: Time evolution of a) monthly mean sea ice extent and b) annual mean sea ice extent anomaly relative to the 1980-2015 average. The sea ice extent is defined as the area (in 10^6 km^2) with sea ice concentration of 15% or higher. The red/blue lines are model results in the northern/ southern hemisphere; black lines are observations from National Snow and Ice Data Center.

Figure 4. a) Time evolution of the modeled monthly mean transport of the Atlantic meridional overturning circulation (AMOC) at 26.5°N; thick line denotes a 10-year averages; b) Variability of the modeled AMOC transports (red line), the observed AMOC transports (black line) from the RAPID array (e.g., Smeed et al., 2018), and the observed meridional heat transport (MHT, blue line) from Trenberth et al. (2019), all in 12-month moving average; c) Seasonal variability of the AMOC transports at 26.56°N averaged over 2004-2017 from model (red line) and the RAPID array (black line).

Figure 5. Observed and modeled distributions of a-b) time mean sea surface height (SSH, in cm), c-d) SSH standard deviation (in cm), and e-f) eddy kinetic energy (EKE, in cm^2 s^{-2}) of the surface current in the southern Atlantic. In observation, the mean SSH is based on long-term climatology CNES-CLS18 (Rio et al., 2019); the SSH standard deviation and EKE are based on AVISO data in 1993-2018. All model results are also in 1993-2018.

Figure 6: Observed and modeled sea-surface height (SSH) anomaly along the Prime Meridian in latitude range 20-40°S from 1993 to 2018. The high SSH anomaly denotes the west-/northwestward translation of the Agulhas Rings that pass the Prime Meridian.

Figure 7. a-d) Potential temperature θ and salinity S distributions across 34°S. Observations are based on a combination of Argo profiles for the top 2000 m and World Ocean Atlas 2013 (WOA13) below 2000 m; model results are from the global 1/12° HYCOM simulation. Three red lines denote isopycnic surfaces (σ_2 of 35.65, 36.58, and 37.12 kg m^{-3}) that divide the water column into near surface water, Antarctic Intermediate Water (AAIW), North Atlantic Deep Water (NADW), and Antarctic Bottom Water (AABW). e-f) Volumetric θ-S diagram along 34°S. Color shading shows the volume percentage for water mass with $\Delta\theta$, ΔS resolution of 0.1°C, 0.02 psu (percentages for near surface water, AAIW, NADW and AABW are also listed); circled lines are volume-weighted θ-S profile in observations (black) and model results (red).

Figure 8. Observed and modeled time mean meridional velocity across 34°S and the corresponding volume transport for the four density layers: near surface water (σ_2<35.65 kg m^{-3}), Antarctic Intermediate Water (AAIW, 35.65<σ_2<36.58), North Atlantic Deep Water (NADW, 36.58< σ_2<37.12), and Antarctic Bottom Water (AABW, σ_2>37.12). Observations are based on a combination of Argo-WOA13 profiles; model results based on the global 1/12° HYCOM simulation.

Figure 9. Long-term mean meridional overturning streamfunction (in Sv) at 34°S with respect to a) depth and b) potential density in σ_2. Observations based on monthly mean Argo-WOA13 profiles; model results based a global 1/12° HYCOM simulation (1979-2018).

Figure 10: a) Time series of the AMOC transport variability (in Sv) at 34°S based on Argo-WOA13 (black, Dong et al., 2014), SAMOC-mooring array (blue, Meinen et al., 2018), and global HYCOM (red). The thin and thick lines represent monthly means and 12-month moving averages, respectively. b) AMOC transport variability at seasonal timescale, with each dot representing the multi-year average of the monthly AMOC transport.

Figure 11: Modeled long-term mean zonal velocity and the corresponding four-layer volume transport in four density layers across a) 65°W in the Drake Passage and b) the Prime Meridian-Good Hope (PM-GH) transect southwest of Africa. The triangles denote the locations of Antarctic circumpolar current (ACC) fronts, from south to north, the Southern Boundary, South ACC Front, Polar Front, Subantarctic Front, and the subtropical front in panel b. The shaded area in panel b) between 40 and 55.5°S marks the ACC regime across the PM-GH transect. Transport is accumulative northward. The four layers are near surface water (σ_2<35.65 kg m^{-3}), Antarctic Intermediate Water (AAIW, 35.65<σ_2<36.58), North Atlantic Deep Water (NADW, 36.58<σ_2<37.12), and Antarctic Bottom Water (AABW, σ_2>37.12).

Figure 12: a) Variability of the modeled ACC transport through the Drake Passage at the 65°W, with thin and thick lines represent monthly means and annual means, respectively; b) Seasonal variability of the modeled ACC transports averaged over 1979-2018.

Figure 13: a) Modeled mean horizontal transports (Sv per 100m) in the vertical across the 34°S, the 65°W, and the PM-GH transects; b) The net transports into the region enclosed by the three transects, with positive (negative) values indicating net transport into (out of) the region.

Figure 14: a) Net transports into the South Atlantic region enclosed by the 34°S, the 65°W, and the PM-GH transects, with respect to density layers (positive/negative values for net transport into/out of the region); b) Solid line denotes the total diapycnal transformation; dashed line denotes the diapycnal transformation calculated from surface buoyancy fluxes.

Figure 15: Modeled long-term mean horizontal transport streamfunction (in Sv) for the layer of near surface water (σ_2<35.65 kg m^{-3}). Red and pink streamlines (increment of 1 Sv) denote AMOC contribution and ACC flow; orange streamlines (increment of 2 Sv) denote the subtropical gyre of the South Atlantic.

Figure 16: Modeled long-term mean horizontal transport streamfunction (Sv) for the layer of AAIW (35.65<σ_2<36.58 kg m^{-3}). Pink streamlines (increment of 4 Sv) is the ACC; red and orange streamlines denote AMOC contribution and the subtropical gyre of the South Atlantic (similar to Figure 15). The dashed blue lines denote 34°S, 45°S, and the GoodHope sections, across which the water properties of the northward and northwestward transports are examined in Figure 17.

Figure 17: Modeled northward transports projected on potential temperature-salinity (θ-S) plane across 6 sections; the transport presented in Sv over an area of (0.2°Cx0.04) in θ-S space. The isopycnal (σ_2) surfaces of 35.65 and 36.58 kg m^{-3} denote the upper and lower AAIW interfaces

Figure 18: a) Probability map of the trajectory occurrence in the South Atlantic (1/4°×1/4° grid) over the 30 year for the 12,554 AAIW particles that were released along 58°W in the Drake Passage (black line) and reached 6°S at the end of integration. The four color lines represent the climatological mean location of the ACC fronts from Orsi et al. (1995): the subantarctic front (SAF, red), polar front (PF, green), southern ACC front (SACCF, blue), and southern boundary of the ACC (SBdy, pink). b) averaged "Lagrangian" AAIW transport from the Drake Passage across seven latitudes as a function of integration time.

Figure 19. Modeled long-term mean horizontal transport streamfunction for the layer of NADW ($36.58<\sigma_2<37.12$ kg m^{-3}). Pink streamlines (10 Sv increment) indicate the eastward transport of the ACC, blue to yellow streamlines (2 Sv increment) represent the southward spreading of the NADW from north.

Figure 20. a) Observed and modeled salinity distribution at 2500m in the South Atlantic. Observations are based on CTD data from GoShip program http://www.go-ship.org. Detailed vertical sections can be seen in the WOCE Atlas (Kiltermann et al., 2011). The results show an eastward extension of high salinity (NADW signature) between 20 and 25°S west of the mid-Atlantic Ridge (MAR), and significantly lower salinity east of MAR.

Figure 21. Zoomed view of the modeled mean circulation for the density layer of NADW ($36.58<\sigma_2<37.12$ kg m^{-3}) across the Mid-Atlantic Ridge in the South Atlantic Ocean.

Figure 22. Power spectral density of the AMOC variability across different latitude bands, showing a lack of distinct period of the variability across all latitudes except on annual timescale.

Figure 23. Modeled seasonal variability of the AMOC transport (in Sv) in the Atlantic basin (35°S-70°N), based on the 3rd Intrinsic mode function (IMF) using the ensemble empirical mode decomposition (EEMD, Wu and Huang 2009). The right panel shows the monthly variability averaged over 1958-2018.

Figure 24. Modeled interannual variability of the AMOC transport (in Sv) in the Atlantic basin (35°S-70°N), based on the 4th and 5th Intrinsic mode function (IMF).

Figure 25. Correlation coefficient between the variability of the domain averaged AMOC transport and the variability of the AMOC transport at each latitude; Red and green are interannual variability (4th and 5th IMF) shown in Figure 24 and blue is decadal variability (6th IMF) shown in Figure 26.

Figure 26. Modeled decadal and longer-term variability of the AMOC transport (in Sv) in the Atlantic Basin (35°S-70°N), based on the 6th and the sum of 7th to 9th Intrinsic mode function (IMF), respectively.

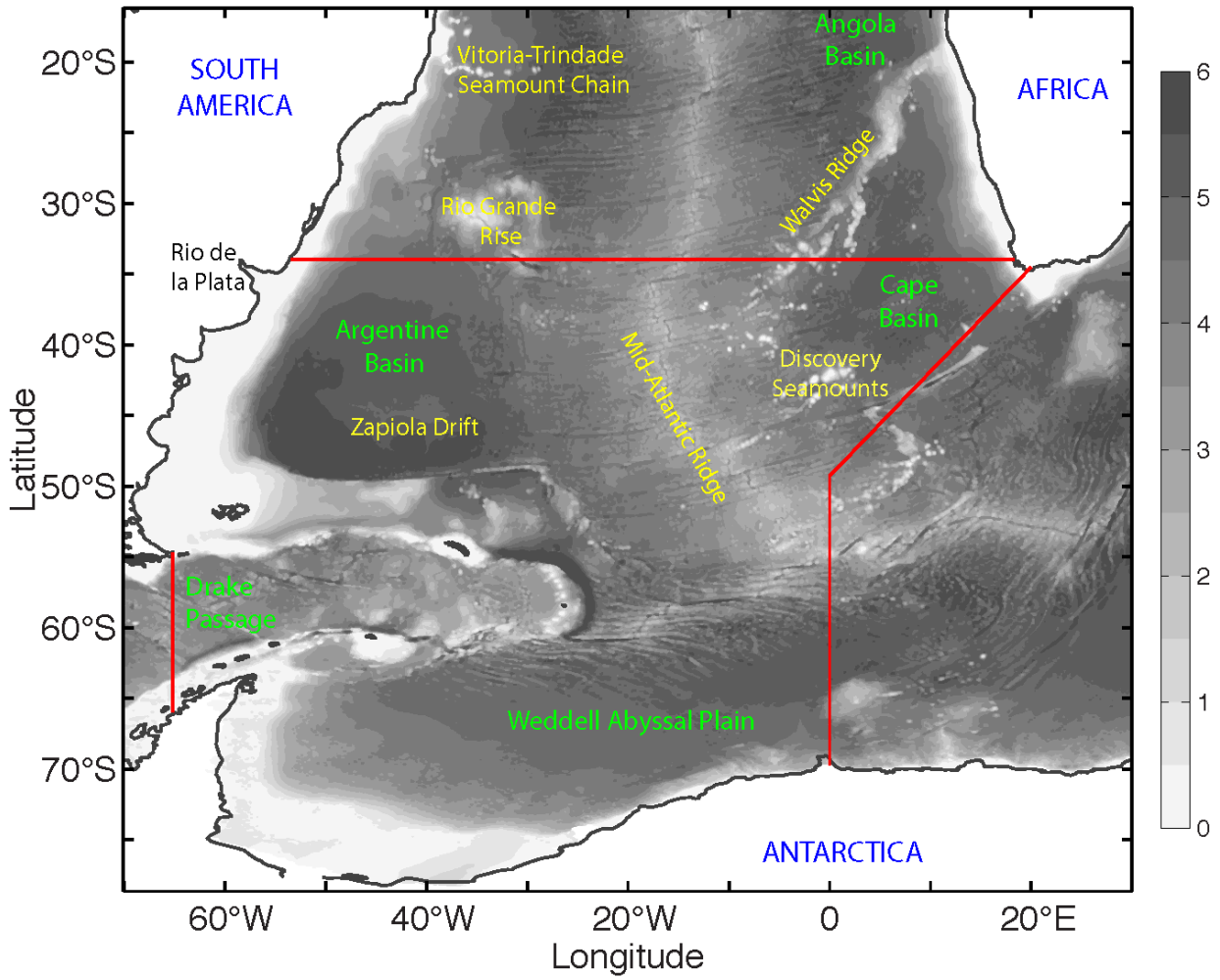

Figure 1: Model bathymetry (in km) along with key topographic features in the South Atlantic Ocean. Red lines denote three sections where significant observations have been obtained and the observations are used to evaluate the model results: 34°S in the South Atlantic, 65°W in Drake Passage, and the Prime Meridian-Good Hope (PM-GH) transect southwest of Africa.

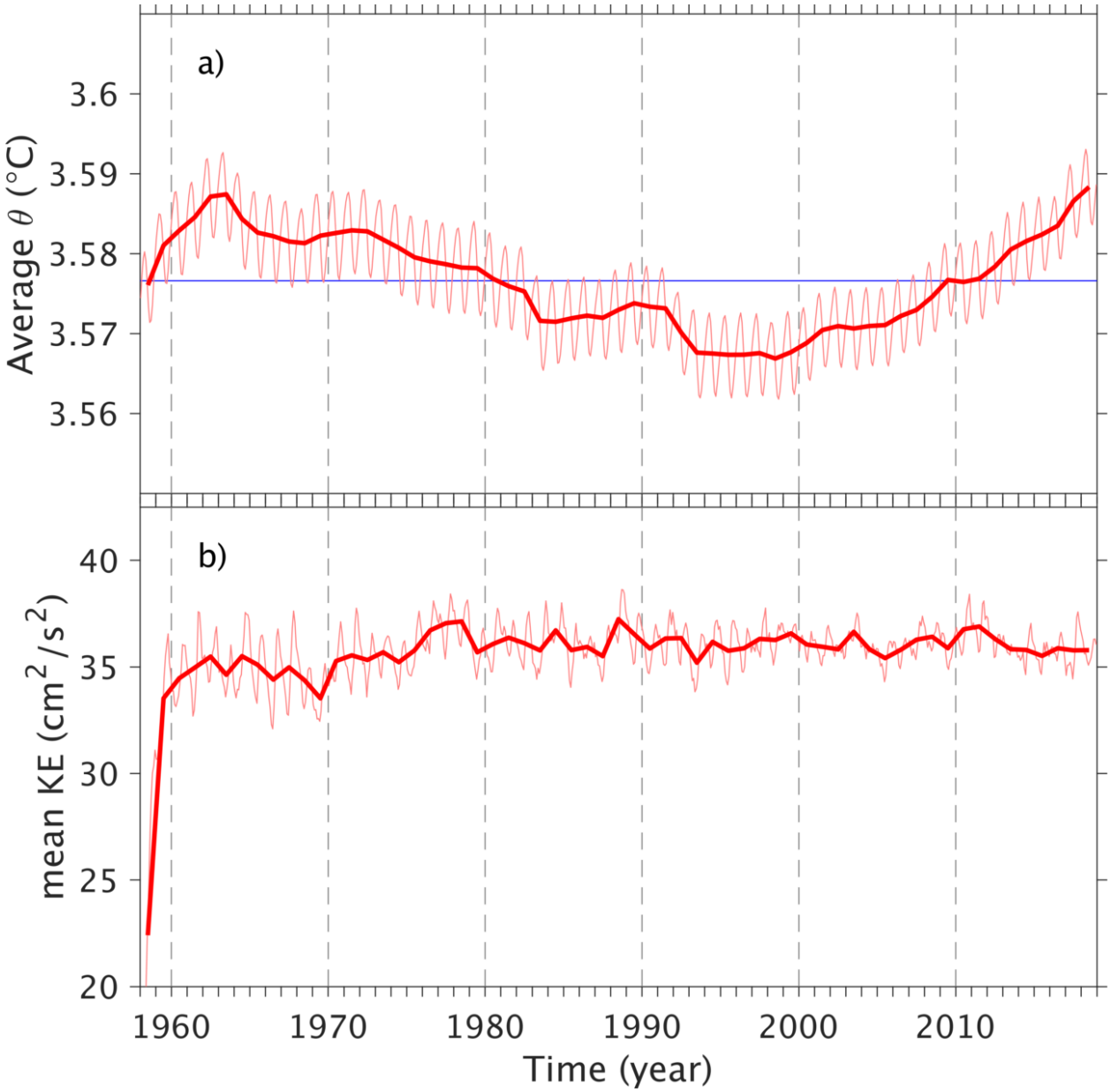

Figure 2: Time evolution of global domain-averaged a) potential temperature in °C and b) total kinetic energy in cm^2s^{-2} from the global ocean-sea ice simulation. Thin and thick lines denote monthly and annual means, respectively.

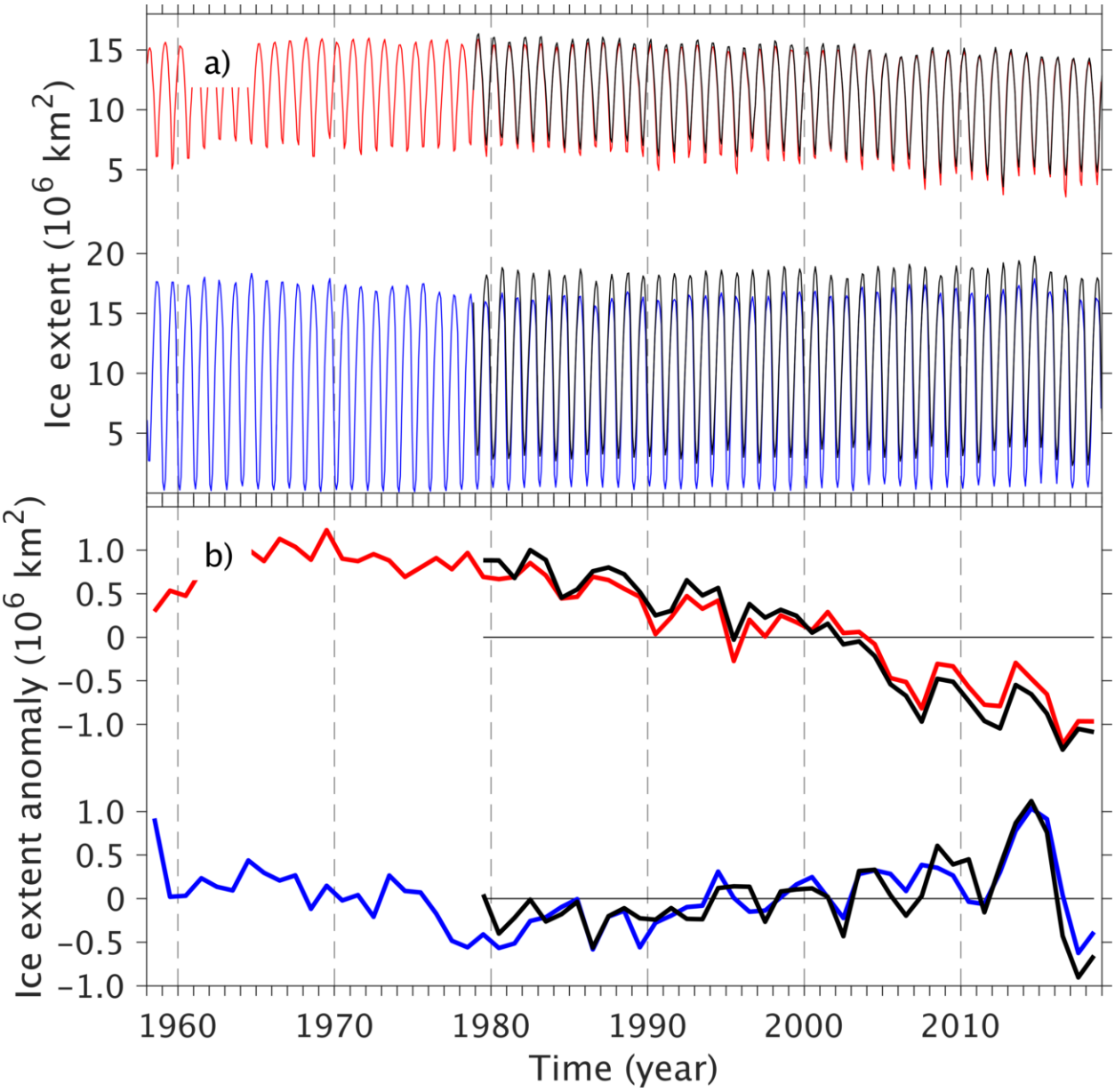

Figure 3: Time evolution of a) monthly mean sea ice extent and b) annual mean sea ice extent anomaly relative to the 1980-2015 average. The sea ice extent is defined as the area (in 10^6 km^2) with sea ice concentration of 15% or higher. The red/blue lines are model results in the northern/ southern hemisphere; black lines are observations from National Snow and Ice Data Center.

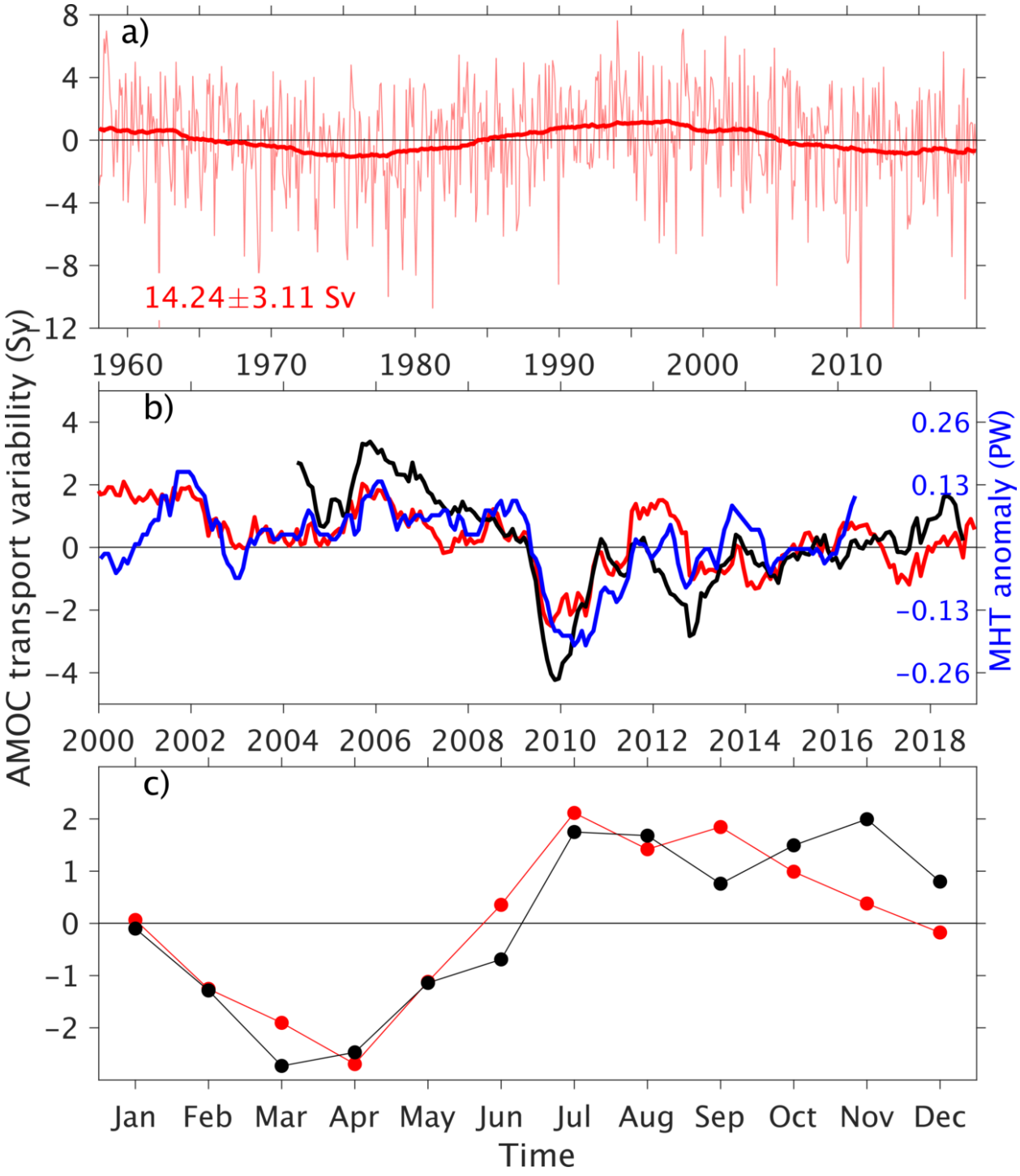

Figure 4. a) Time evolution of the modeled monthly mean transport of the Atlantic meridional overturning circulation (AMOC) at 26.5°N; thick line denotes a 10-year averages; b) Variability of the modeled AMOC transports (red line), the observed AMOC transports (black line) from the RAPID array (e.g., Smeed et al., 2018), and the observed meridional heat transport (MHT, blue line) from Trenberth et al. (2019), all in 12-month moving average; c) Seasonal variability of the AMOC transports at 26.56°N averaged over 2004-2017 from model (red line) and the RAPID array (black line).

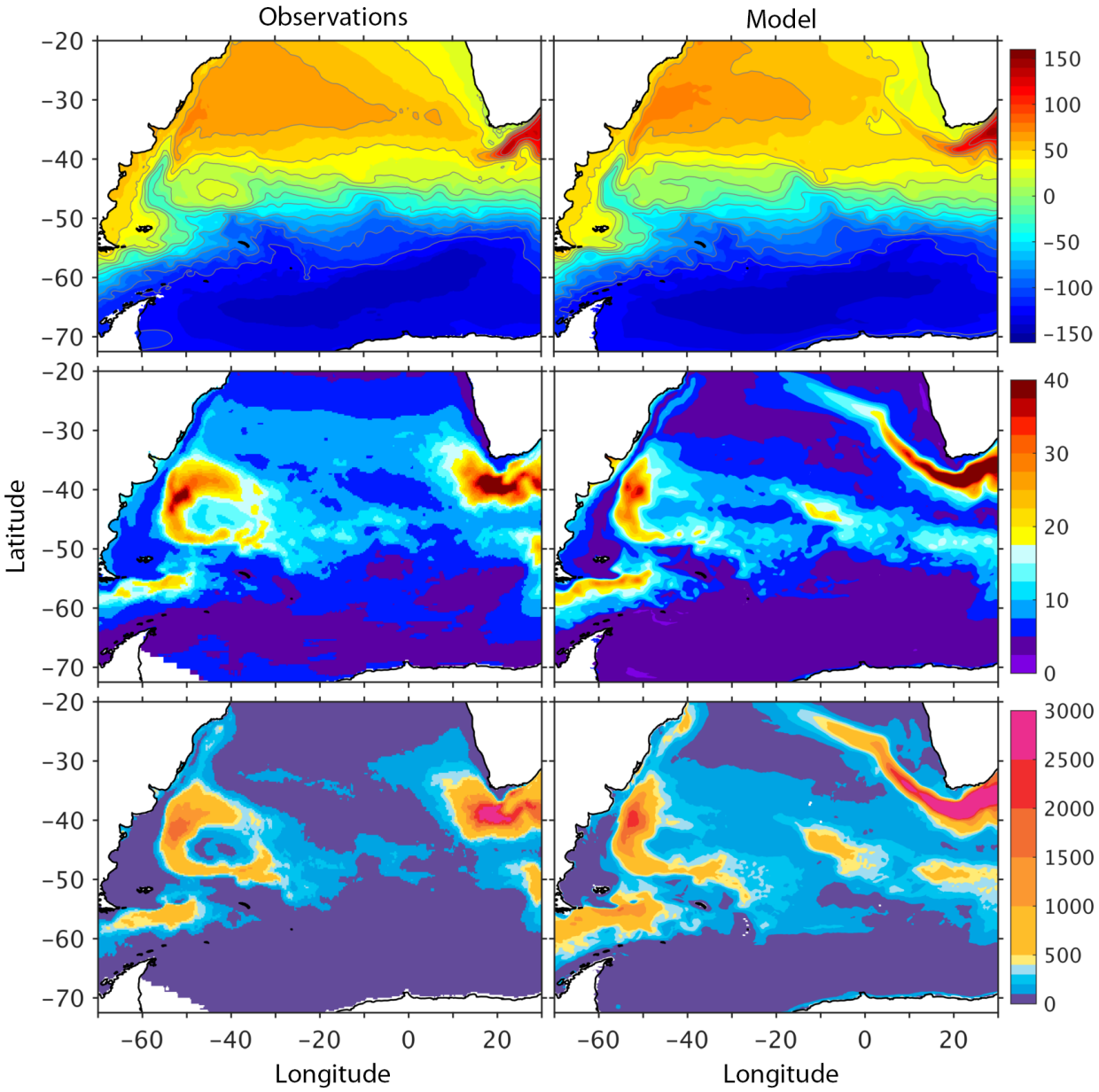

Figure 5. Observed and modeled distributions of a-b) time mean sea surface height (SSH, in cm), c-d) SSH standard deviation (in cm), and e-f) eddy kinetic energy (EKE, in $cm^2\ s^{-2}$) of the surface current in the southern Atlantic. In observation, the mean SSH is based on long-term climatology CNES-CLS18 (Rio et al., 2019); the SSH standard deviation and EKE are based on AVISO data in 1993-2018. All model results are also in 1993-2018.

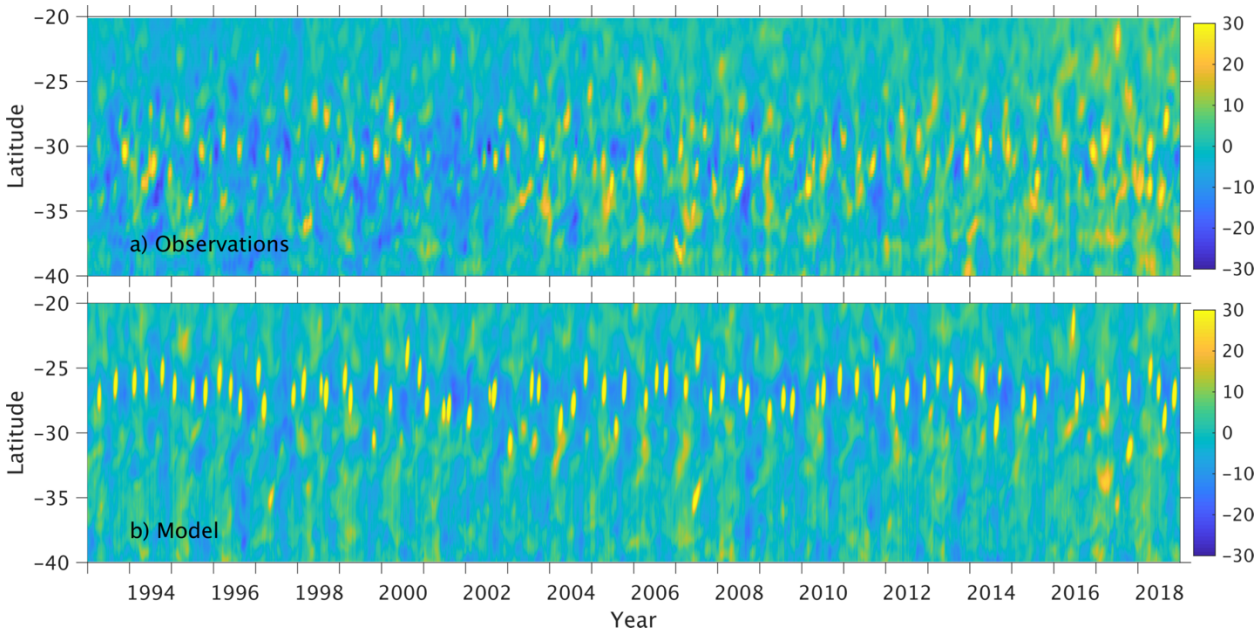

Figure 6: Observed and modeled sea-surface height (SSH) anomaly along the Prime Meridian in latitude range 20-40°S from 1993 to 2018. The high SSH anomaly denotes the west-/northwestward translation of the Agulhas Rings that pass the Prime Meridian.

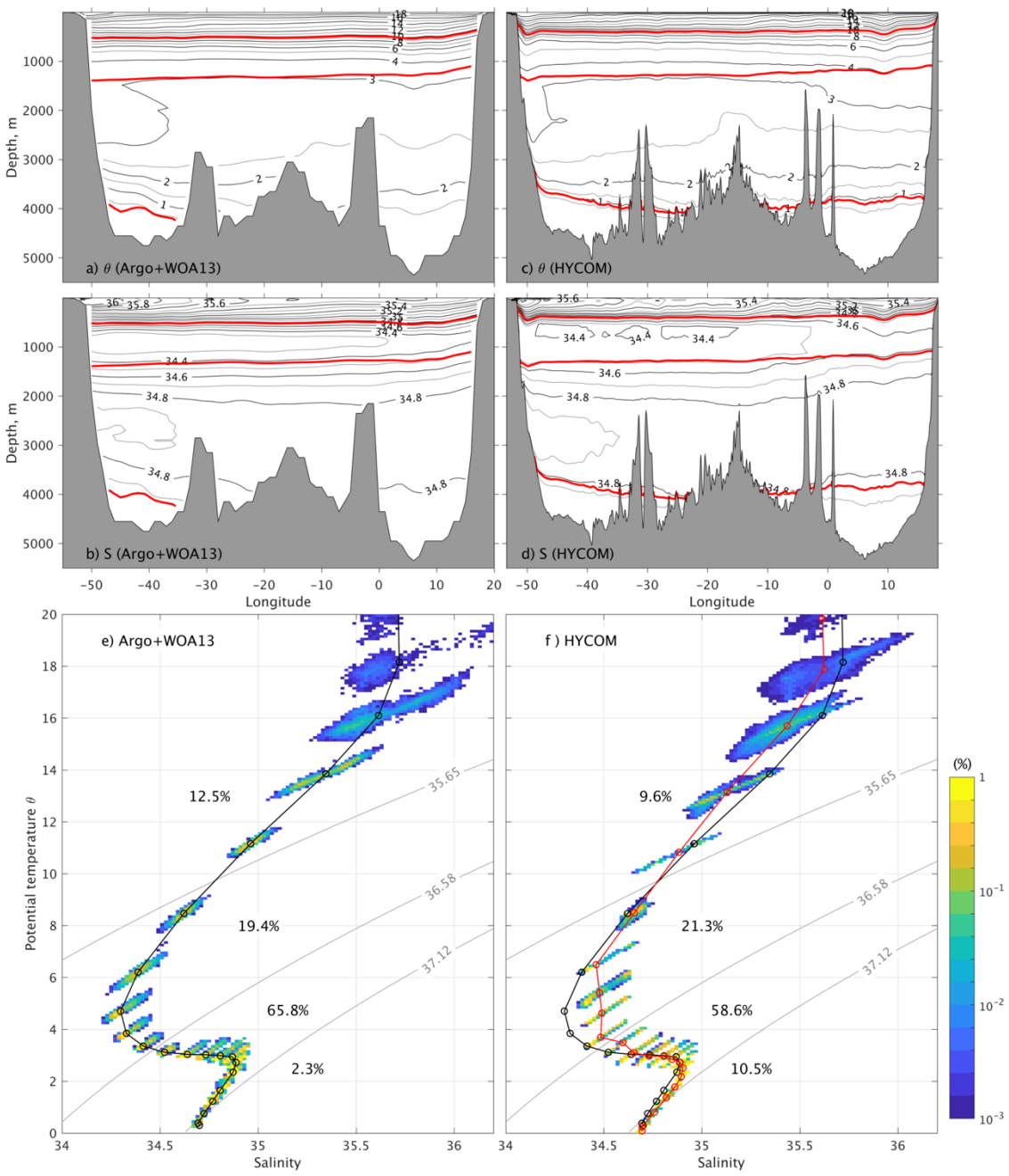

Figure 7. a-d) Potential temperature θ and salinity S distributions across 34°S. Observations are based on a combination of Argo profiles for the top 2000 m and World Ocean Atlas 2013 (WOA13) below 2000 m; model results are from the global 1/12° HYCOM simulation. Three red lines denote isopycnic surfaces (σ_2 of 35.65, 36.58, and 37.12 kg m^{-3}) that divide the water column into near surface water, Antarctic Intermediate Water (AAIW), North Atlantic Deep Water (NADW), and Antarctic Bottom Water (AABW). e-f) Volumetric θ-S diagram along 34°S. Color shading shows the volume percentage for water mass with $\Delta\theta$, ΔS resolution of 0.1°C, 0.02 psu (percentages for near surface water, AAIW, NADW and AABW are also listed); circled lines are volume-weighted θ-S profile in observations (black) and model results (red).

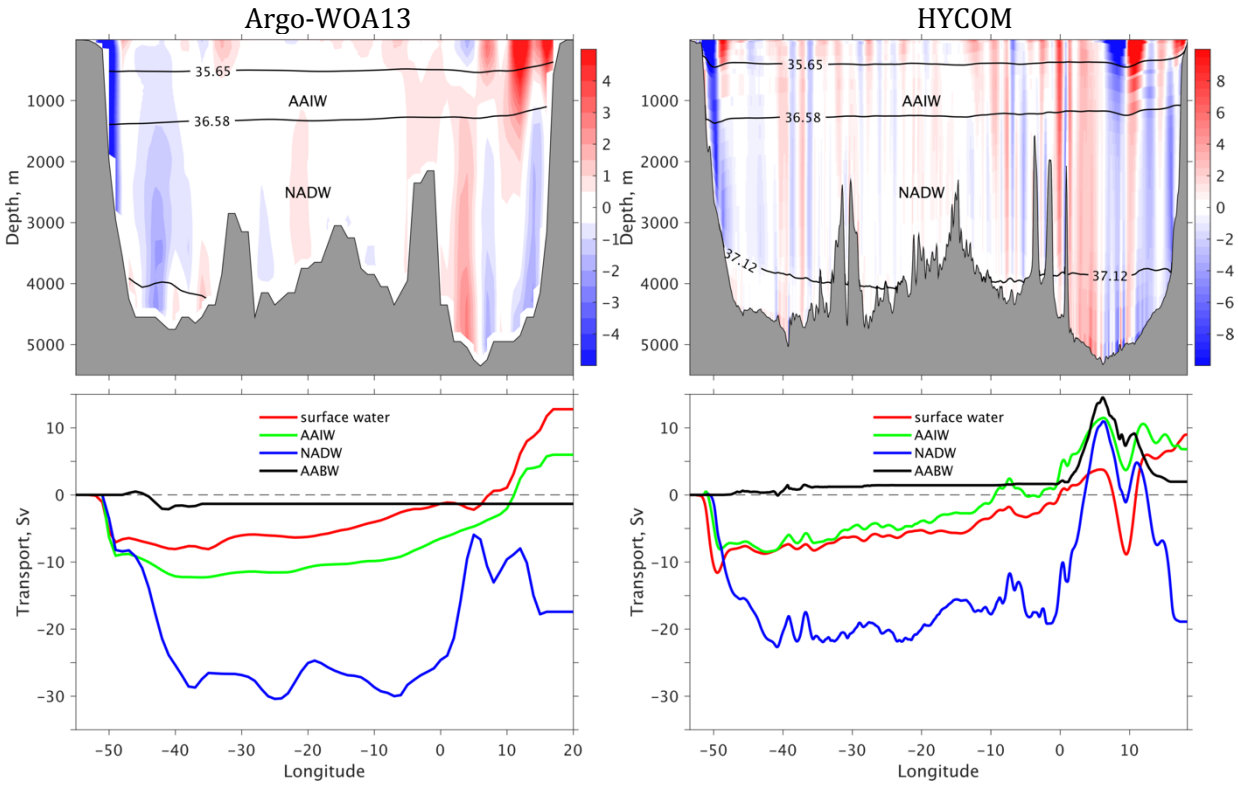

Figure 8. Observed and modeled time mean meridional velocity across 34°S and the corresponding volume transport for the four density layers: near surface water (σ_2<35.65 kg m^{-3}), Antarctic Intermediate Water (AAIW, 35.65<σ_2<36.58), North Atlantic Deep Water (NADW, 36.58< σ_2<37.12), and Antarctic Bottom Water (AABW, σ_2>37.12). Observations are based on a combination of Argo-WOA13 profiles; model results based on the global 1/12° HYCOM simulation.

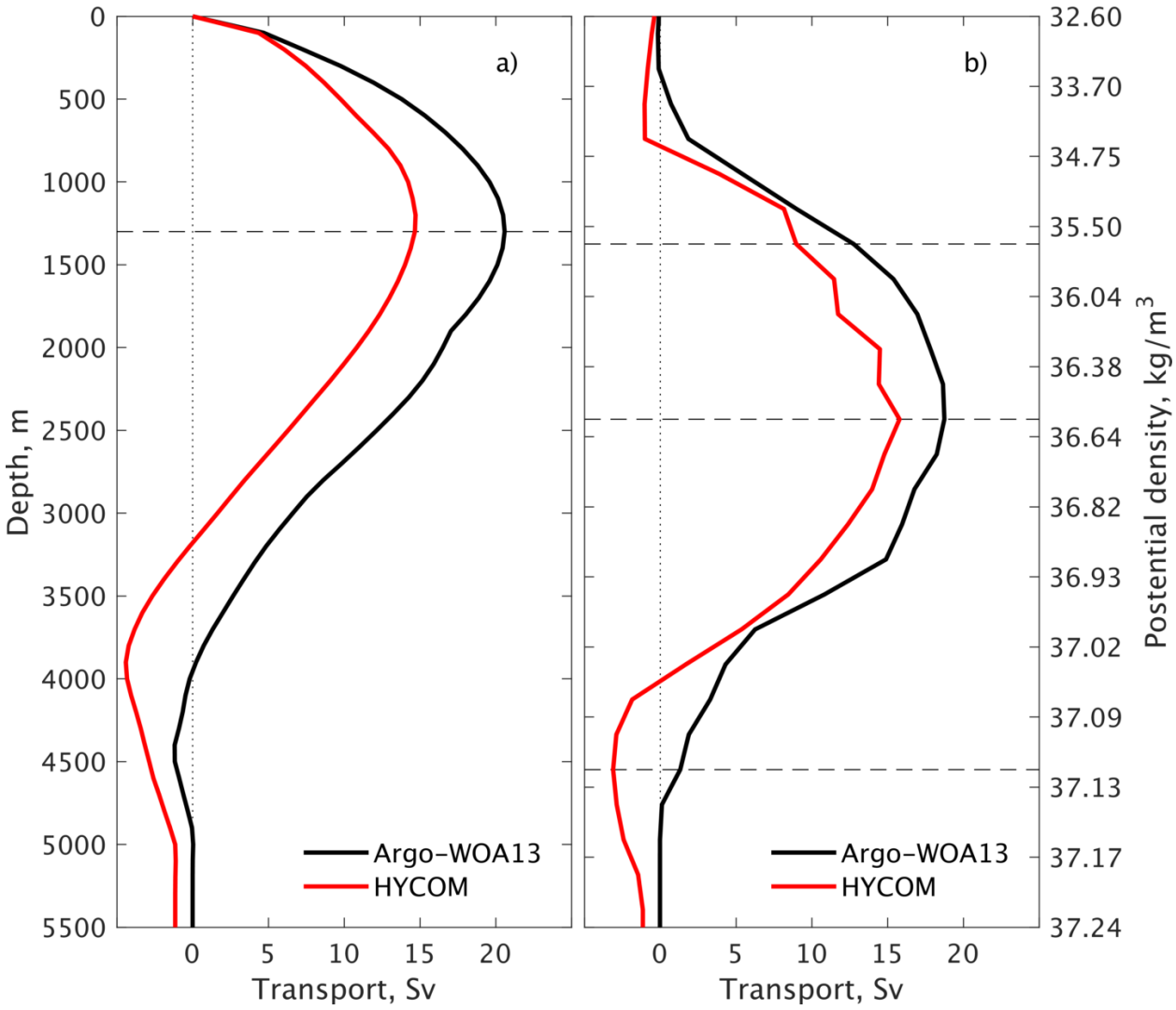

Figure 9. Long-term mean meridional overturning streamfunction (in Sv) at 34°S with respect to a) depth and b) potential density in σ_2. Observations based on monthly mean Argo-WOA13 profiles; model results based a global 1/12° HYCOM simulation (1979-2018).

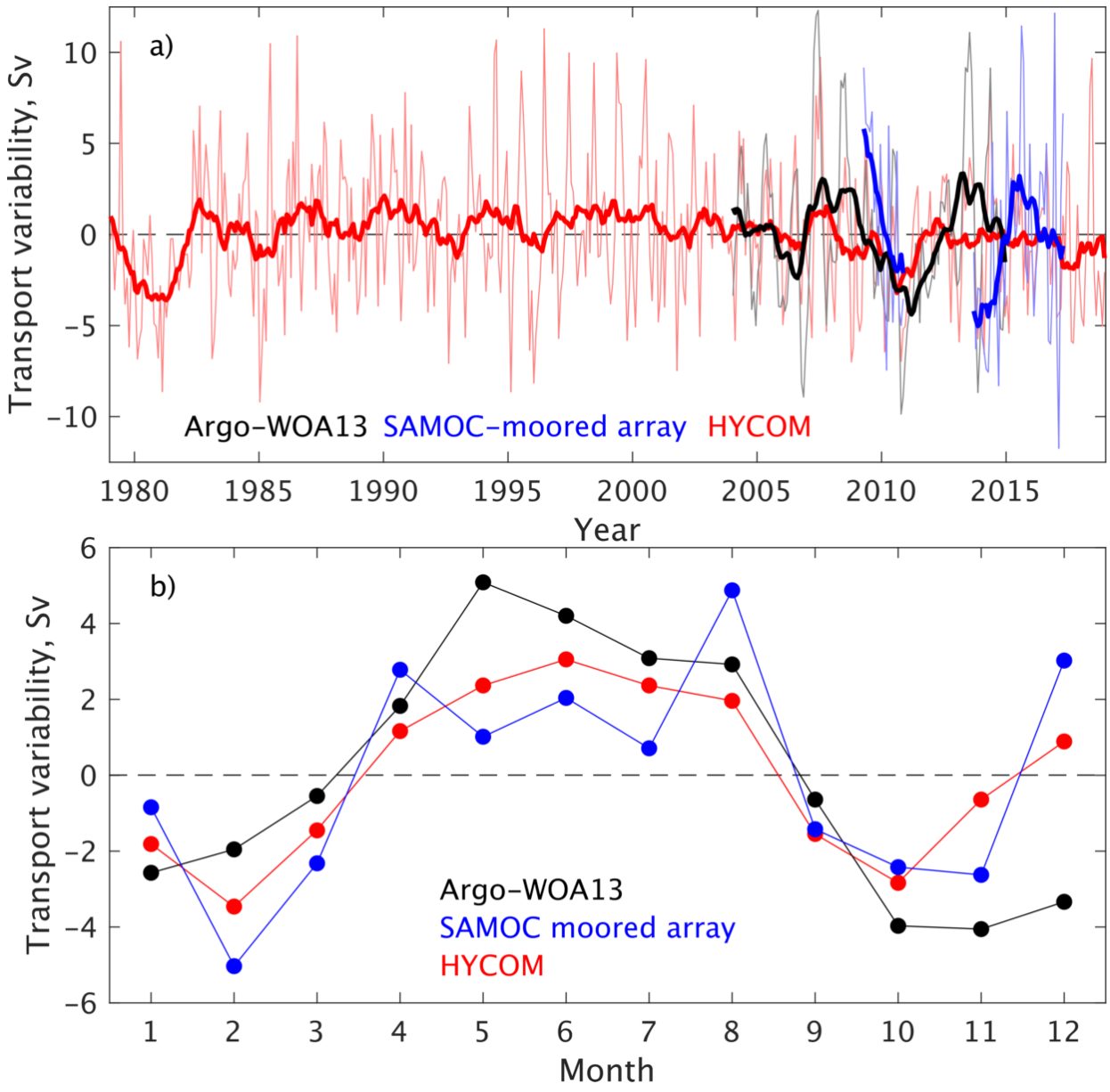

Figure 10: a) Time series of the AMOC transport variability (in Sv) at 34°S based on Argo-WOA13 (black, Dong et al., 2014), SAMOC-mooring array (blue, Meinen et al., 2018), and global HYCOM (red). The thin and thick lines represent monthly means and 12-month moving averages, respectively. b) AMOC transport variability at seasonal timescale, with each dot representing the multi-year average of the monthly AMOC transport.

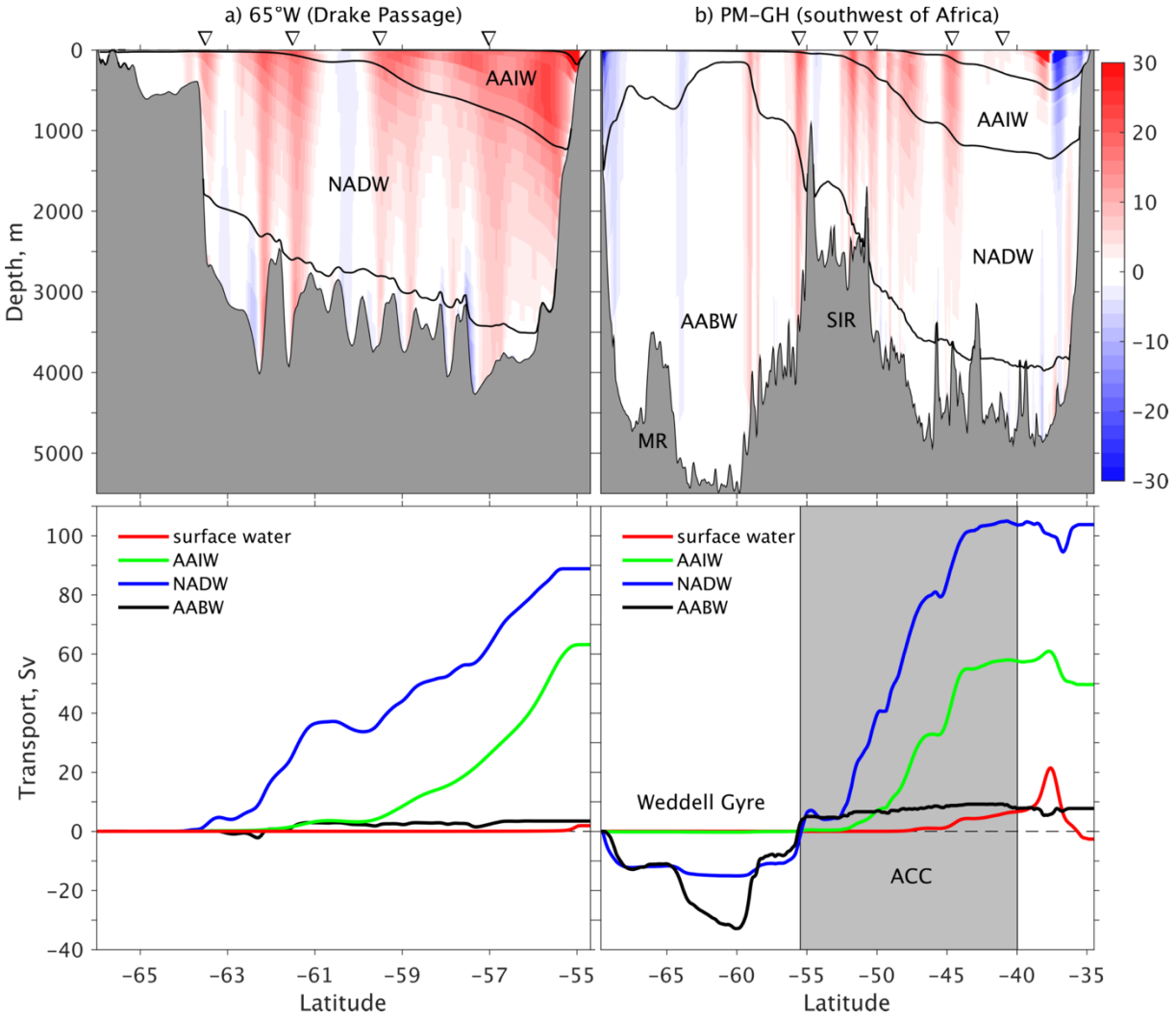

Figure 11: Modeled long-term mean zonal velocity and the corresponding four-layer volume transport in four density layers across a) 65°W in the Drake Passage and b) the Prime Meridian-Good Hope (PM-GH) transect southwest of Africa. The triangles denote the locations of Antarctic circumpolar current (ACC) fronts, from south to north, the Southern Boundary, South ACC Front, Polar Front, Subantarctic Front, and the subtropical front in panel b. The shaded area in panel b) between 40 and 55.5°S marks the ACC regime across the PM-GH transect. Transport is accumulative northward. The four layers are near surface water (σ_2<35.65 kg m^{-3}), Antarctic Intermediate Water (AAIW, 35.65<σ_2<36.58), North Atlantic Deep Water (NADW, 36.58<σ_2<37.12), and Antarctic Bottom Water (AABW, σ_2>37.12).

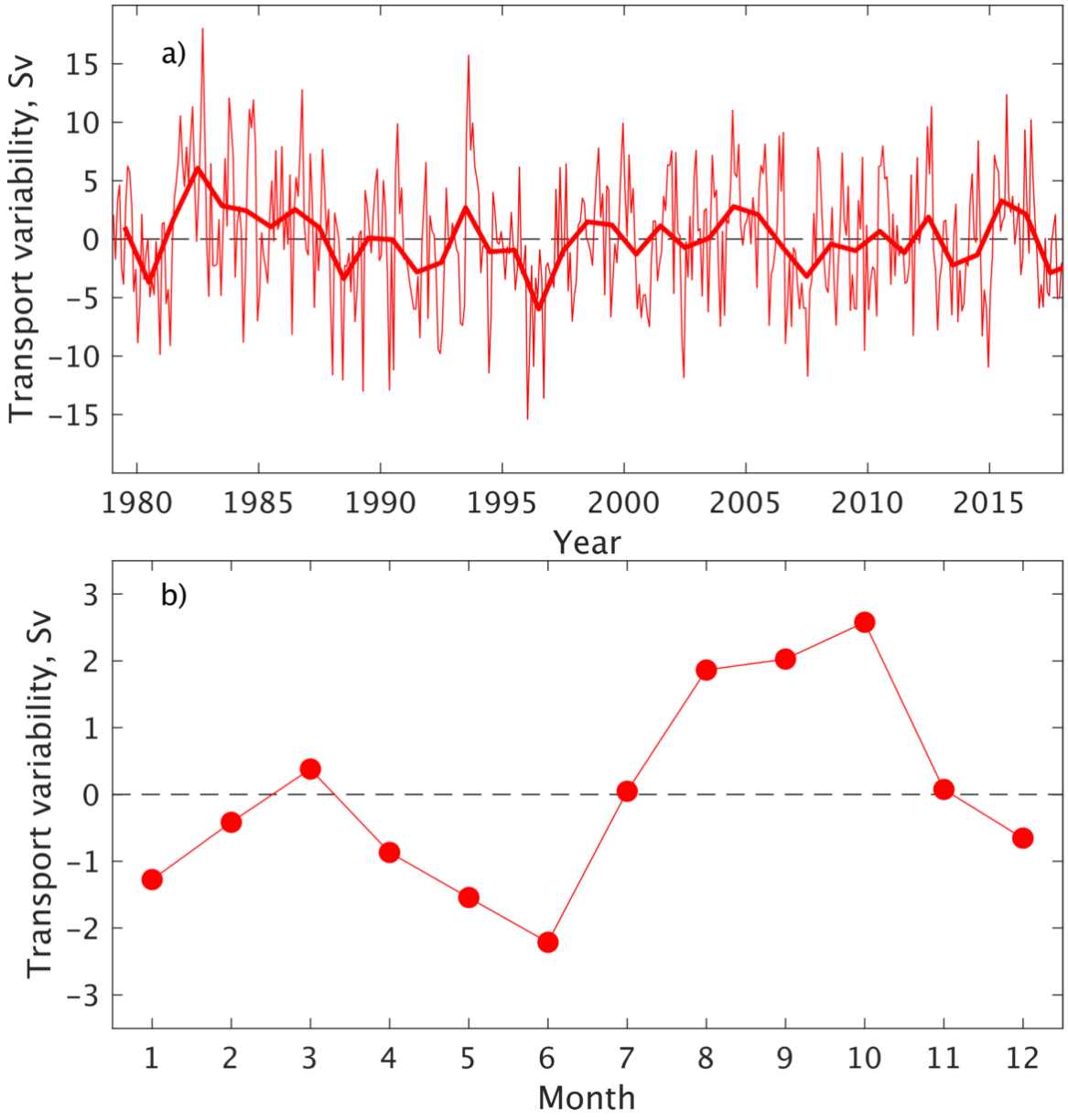

Figure 12: a) Variability of the modeled ACC transport through the Drake Passage at the 65°W, with thin and thick lines represent monthly means and annual means, respectively; b) Seasonal variability of the modeled ACC transports averaged over 1979-2018.

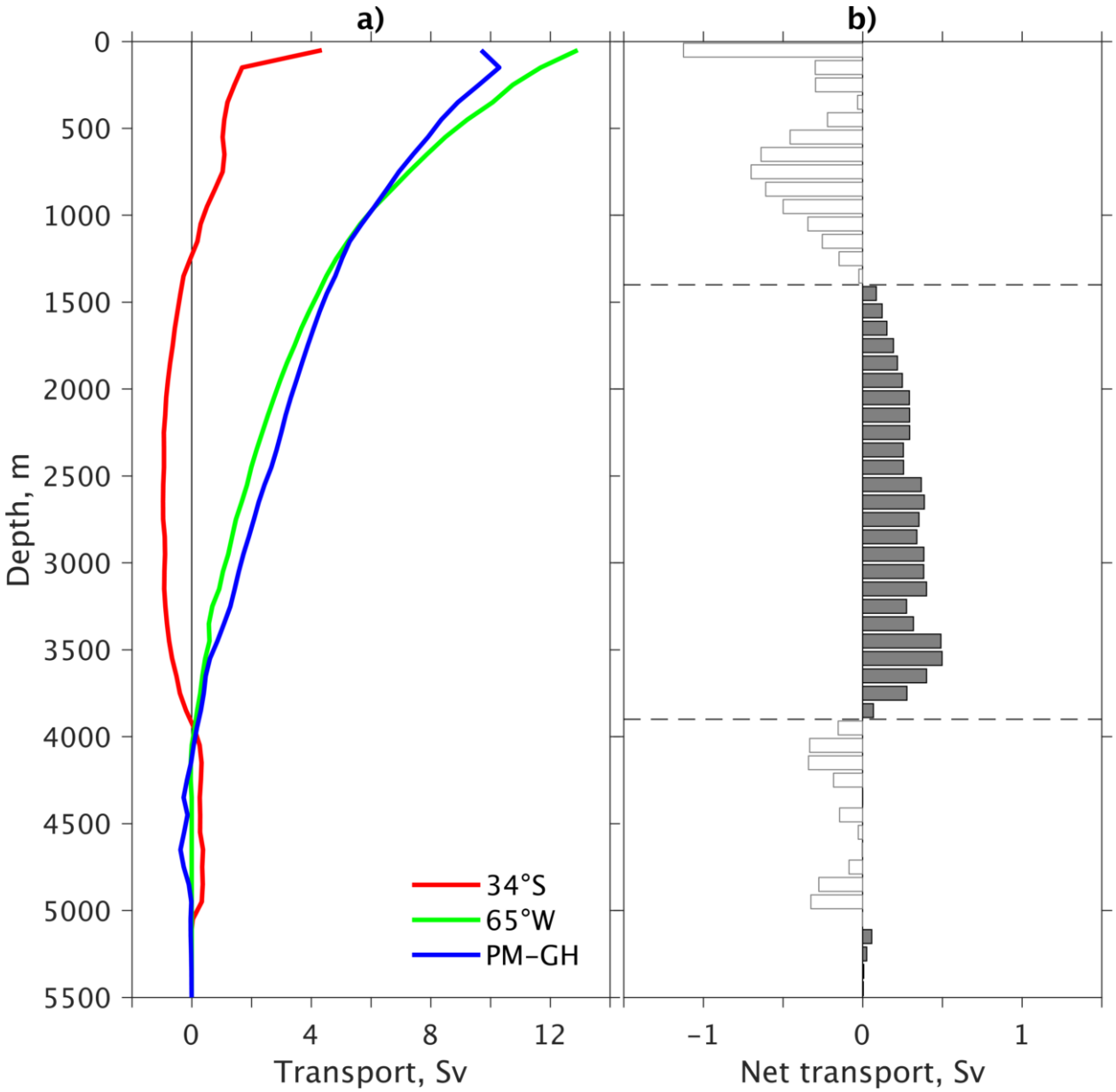

Figure 13: a) Modeled mean horizontal transports (Sv per 100m) in the vertical across the 34°S, the 65°W, and the PM-GH transects; b) The net transports into the region enclosed by the three transects, with positive (negative) values indicating net transport into (out of) the region.

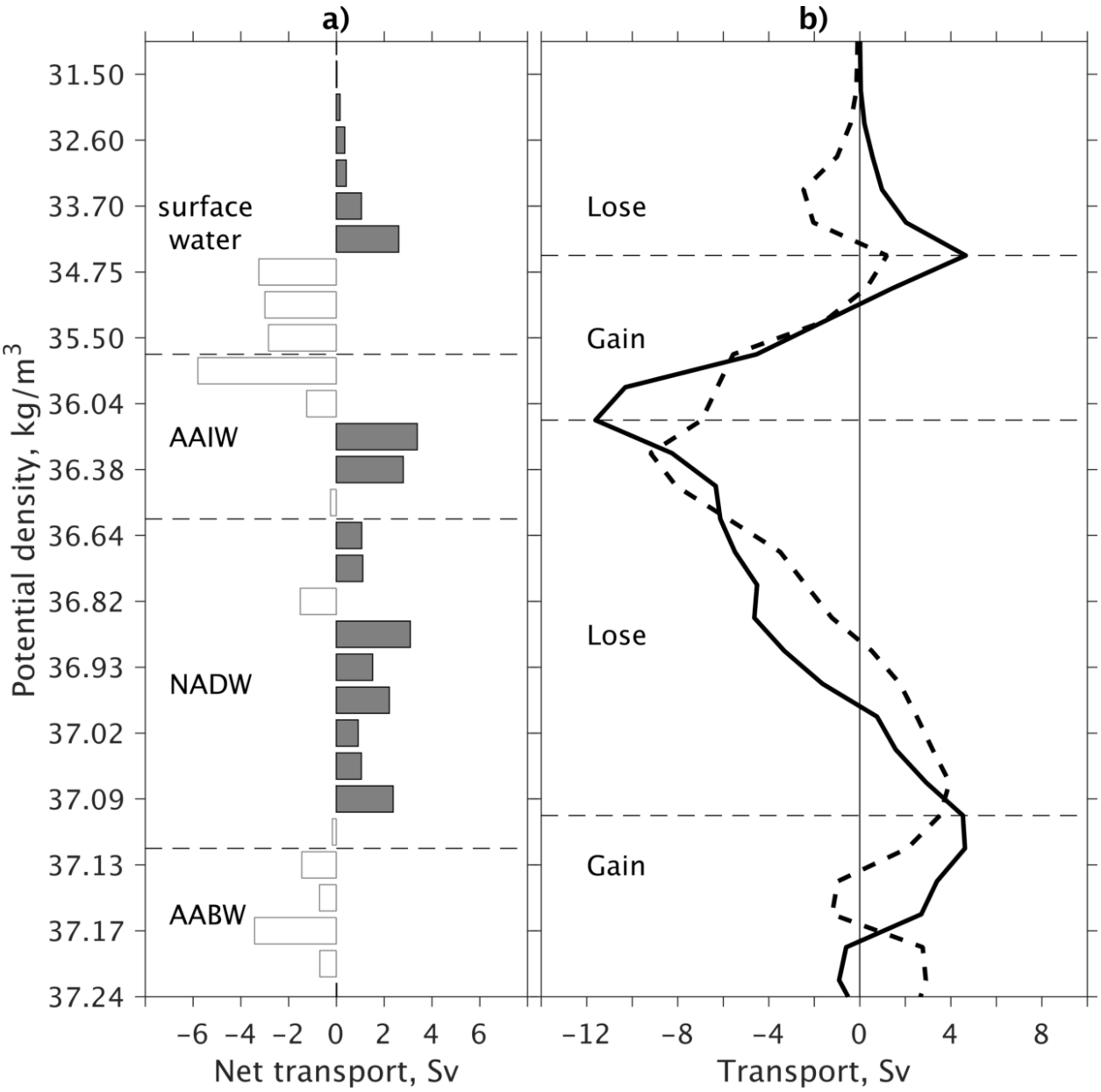

Figure 14: a) Net transports into the South Atlantic region enclosed by the 34°S, the 65°W, and the PM-GH transects, with respect to density layers (positive/negative values for net transport into/out of the region); b) Solid line denotes the total diapycnal transformation; dashed line denotes the diapycnal transformation calculated from surface buoyancy fluxes.

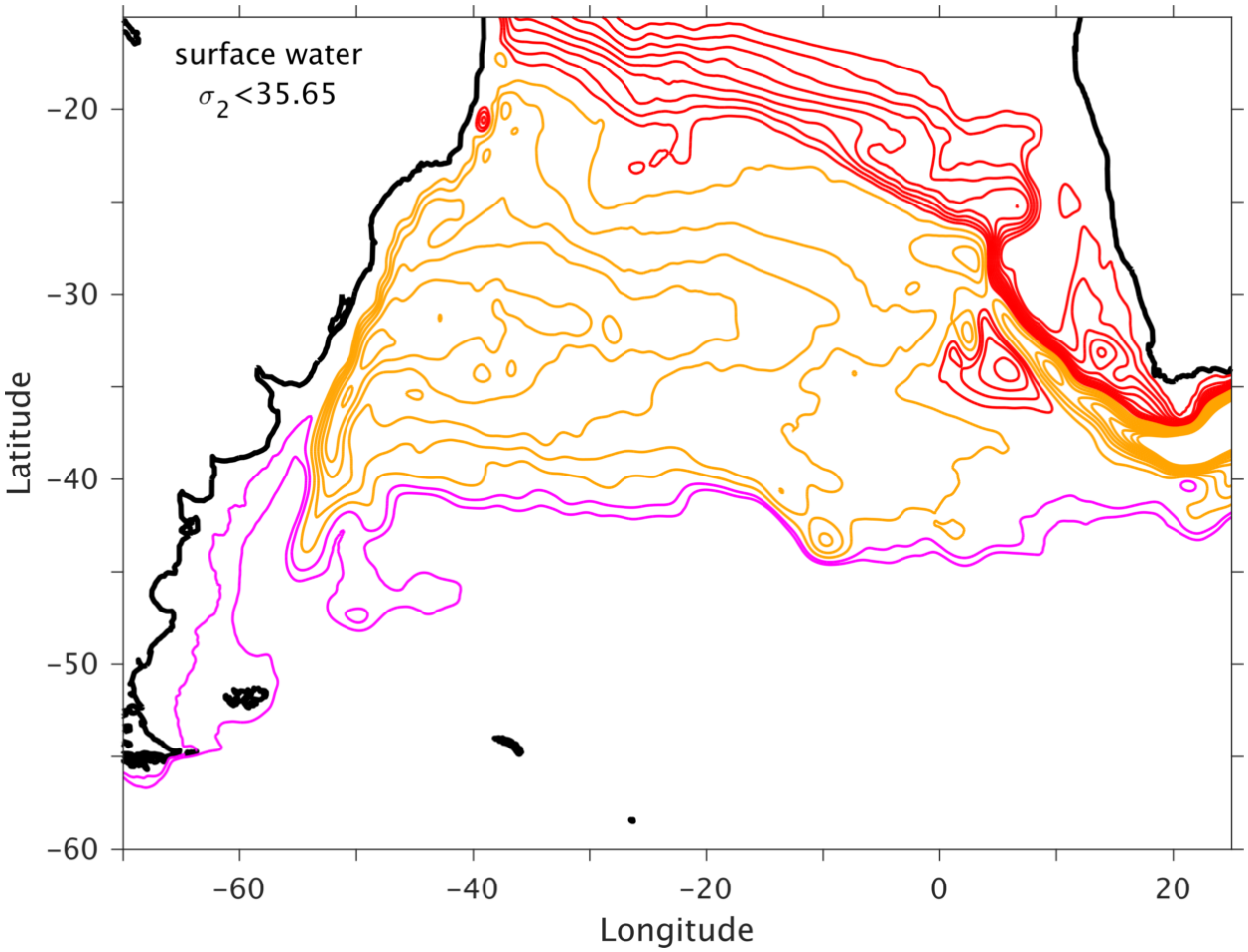

Figure 15: Modeled long-term mean horizontal transport streamfunction (in Sv) for the layer of near surface water (σ_2<35.65 kg m^{-3}). Red and pink streamlines (increment of 1 Sv) denote AMOC contribution and ACC flow; orange streamlines (increment of 2 Sv) denote the subtropical gyre of the South Atlantic.

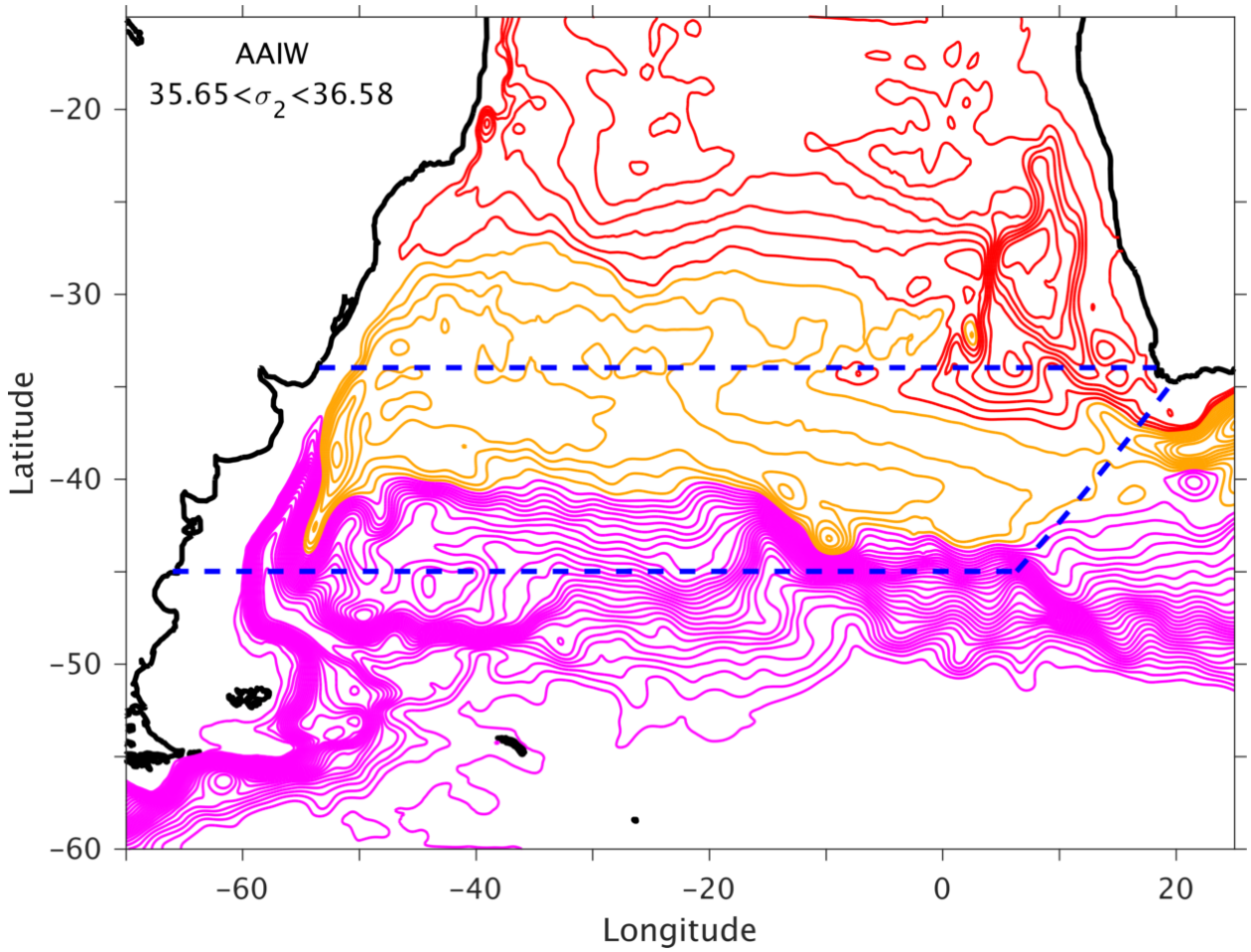

Figure 16: Modeled long-term mean horizontal transport streamfunction (Sv) for the layer of AAIW ($35.65<\sigma_2<36.58$ kg m^{-3}). Pink streamlines (increment of 4 Sv) is the ACC; red and orange streamlines denote AMOC contribution and the subtropical gyre of the South Atlantic (similar to Figure 15). The dashed blue lines denote 34°S, 45°S, and the GoodHope sections, across which the water properties of the northward and northwestward transports are examined in Figure 17.

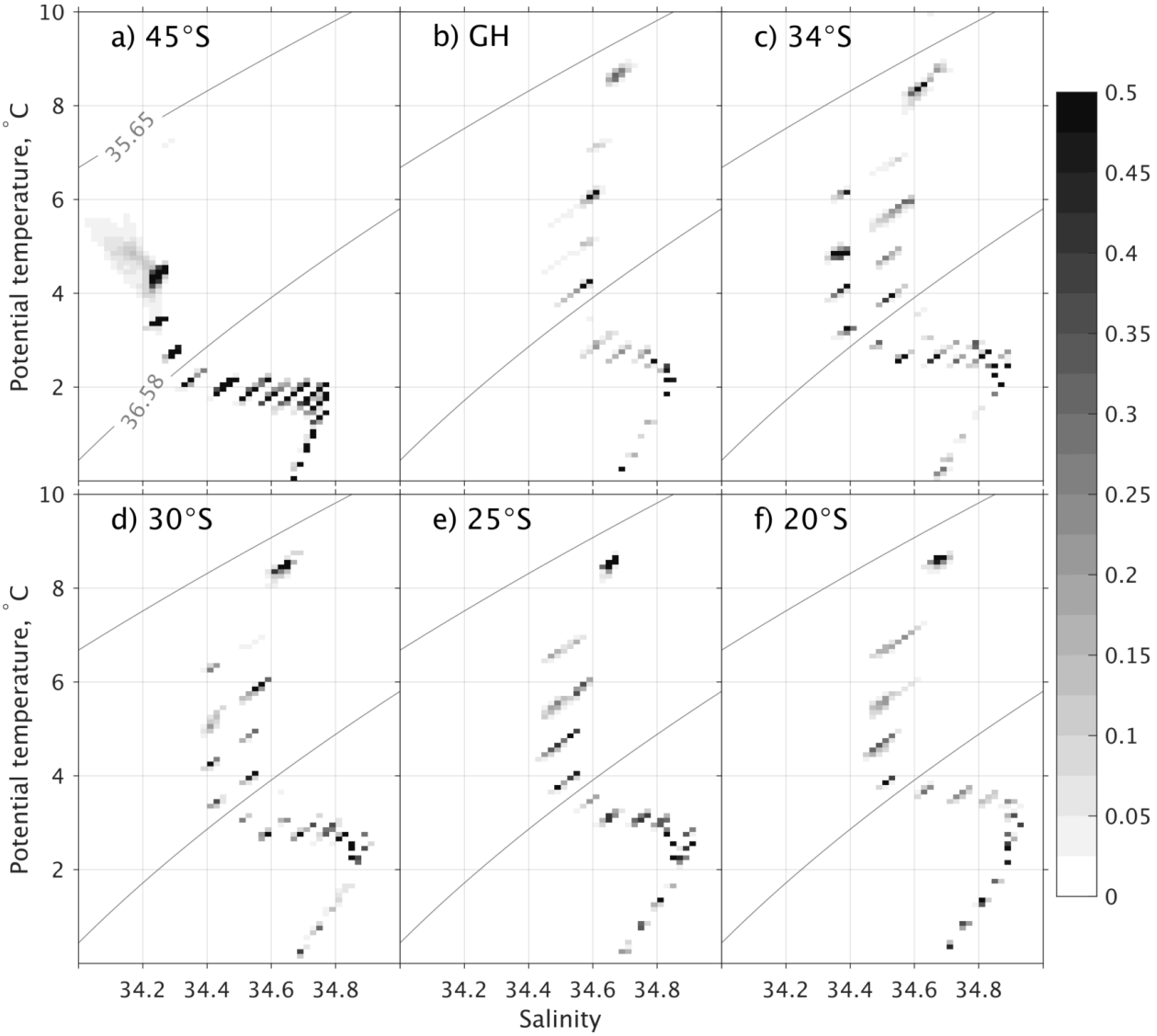

Figure 17: Modeled northward transports projected on potential temperature-salinity (θ-S) plane across 6 sections; the transport presented in Sv over an area of (0.2°Cx0.04) in θ-S space. The isopycnal (σ_2) surfaces of 35.65 and 36.58 kg m^{-3} denote the upper and lower AAIW interfaces.

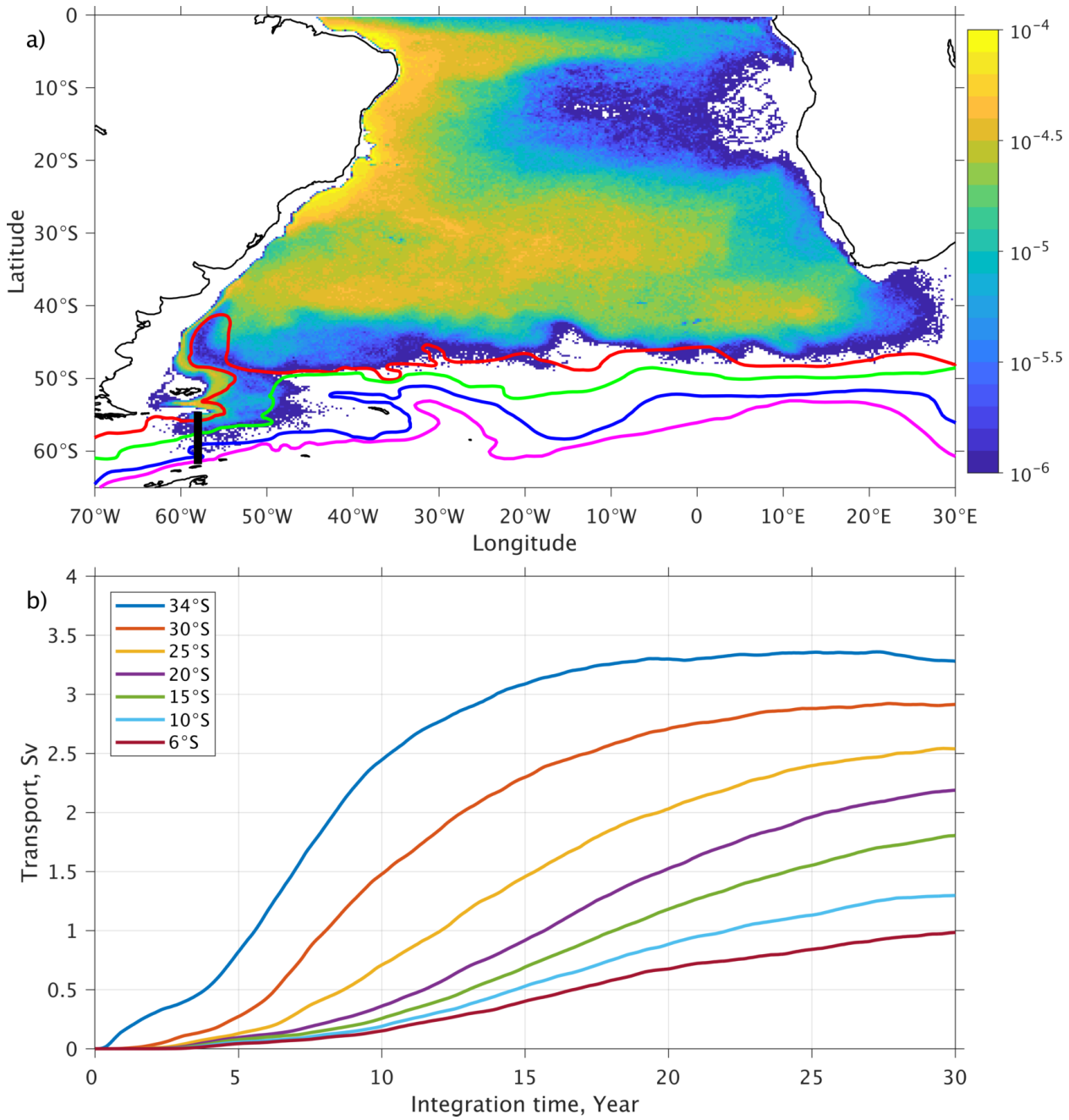

Figure 18: a) Probability map of the trajectory occurrence in the South Atlantic (1/4°×1/4° grid) over the 30 year for the 12,554 AAIW particles that were released along 58°W in the Drake Passage (black line) and reached 6°S at the end of integration. The four color lines represent the climatological mean location of the ACC fronts from Orsi et al. (1995): the subantarctic front (SAF, red), polar front (PF, green), southern ACC front (SACCF, blue), and southern boundary of the ACC (SBdy, pink). b) averaged "Lagrangian" AAIW transport from the Drake Passage across seven latitudes as a function of integration time.

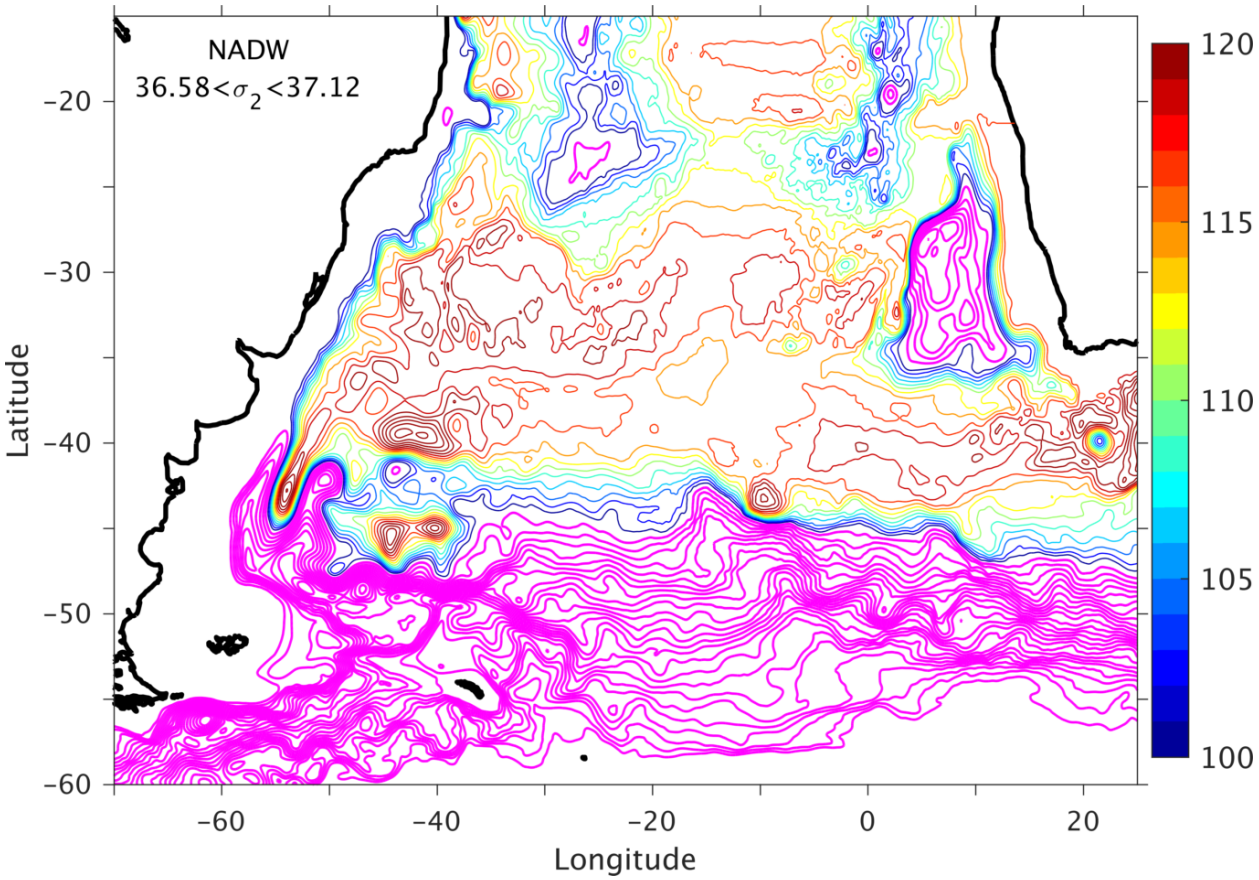

Figure 19. Modeled long-term mean horizontal transport streamfunction for the layer of NADW ($36.58<\sigma_2<37.12$ kg m^{-3}). Pink streamlines (10 Sv increment) indicate the eastward transport of the ACC, blue to yellow streamlines (2 Sv increment) represent the southward spreading of the NADW from north.

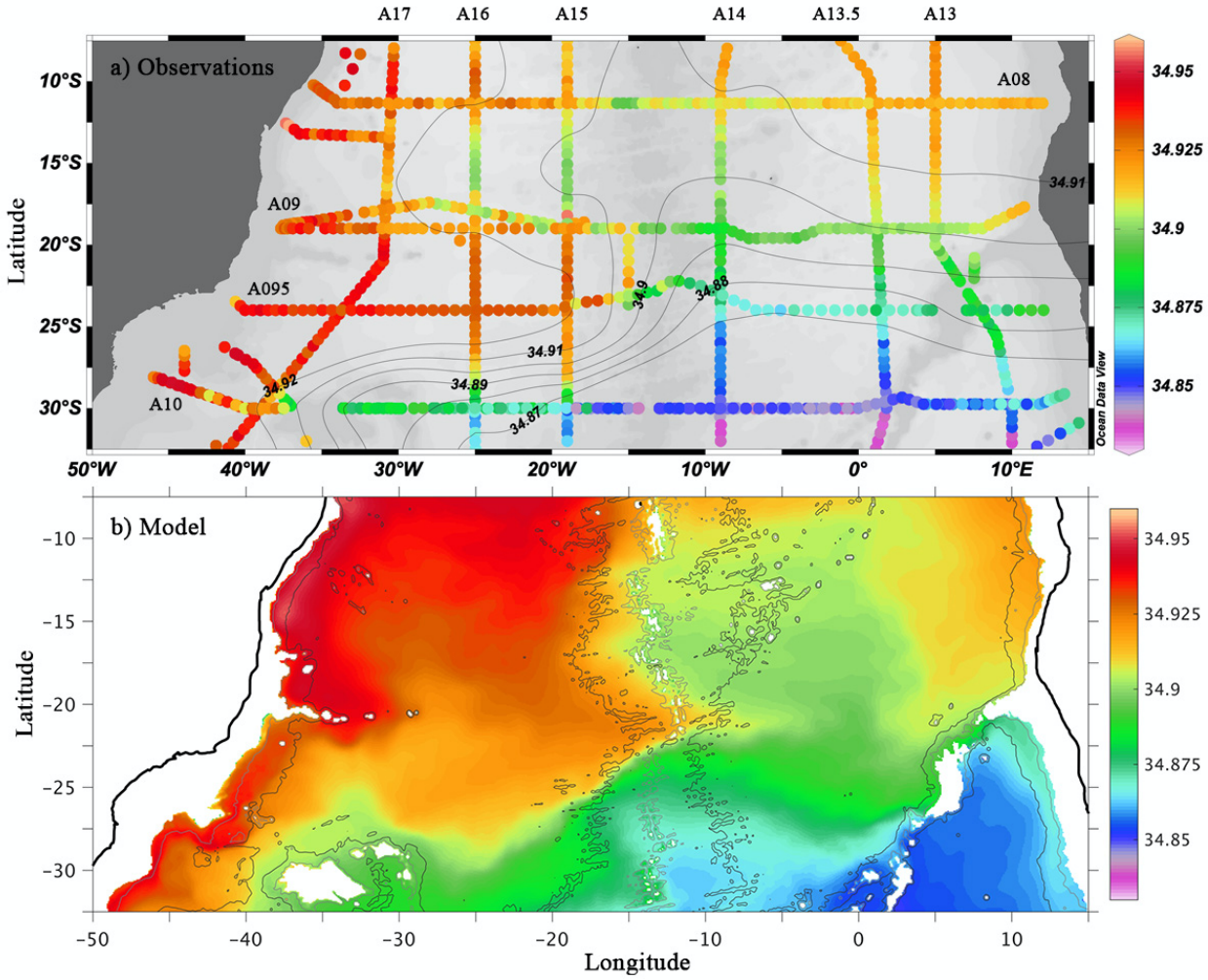

Figure 20. a) Observed and modeled salinity distribution at 2500m in the South Atlantic. Observations are based on CTD data from GoShip program http://www.go-ship.org. Detailed vertical sections can be seen in the WOCE Atlas (Kiltermann et al., 2011). The results show an eastward extension of high salinity (NADW signature) between 20 and 25°S west of the mid-Atlantic Ridge (MAR), and significantly lower salinity east of MAR.

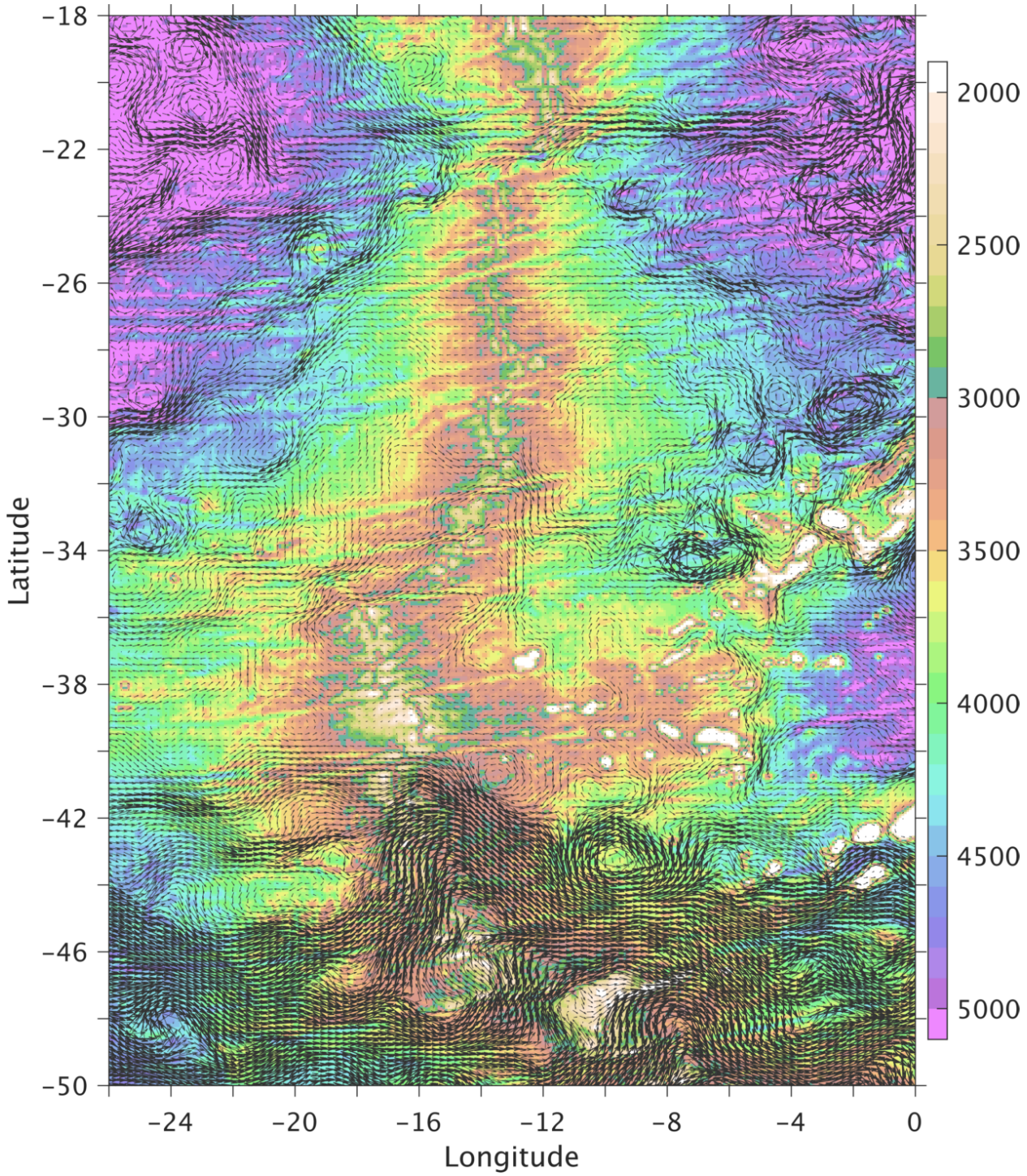

Figure 21. Zoomed view of the modeled mean circulation for the density layer of NADW ($36.58<\sigma_2<37.12$ kg m^{-3}) across the Mid-Atlantic Ridge in the South Atlantic Ocean.

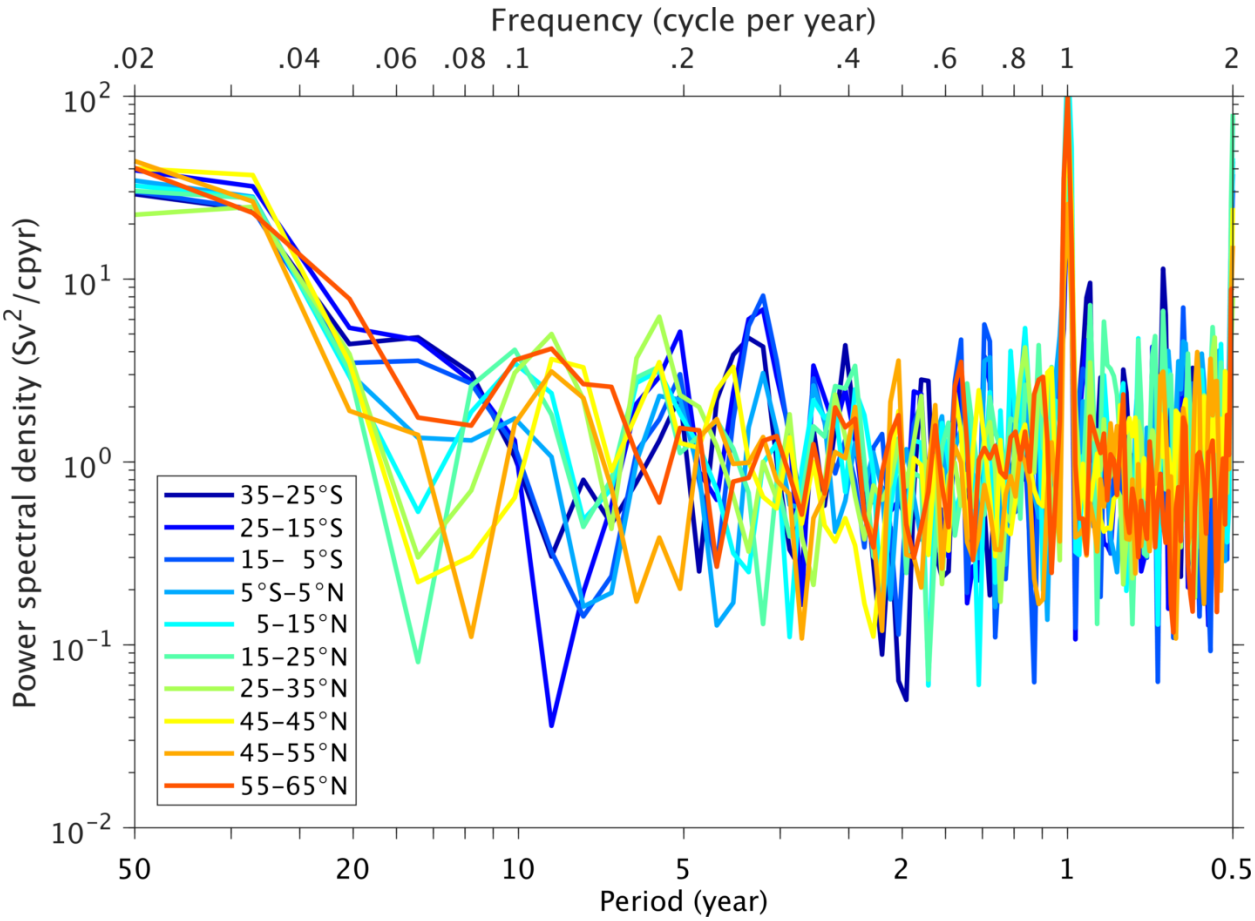

Figure 22. Power spectral density of the AMOC variability across different latitude bands, showing a lack of distinct period of the variability across all latitudes except on annual timescale.

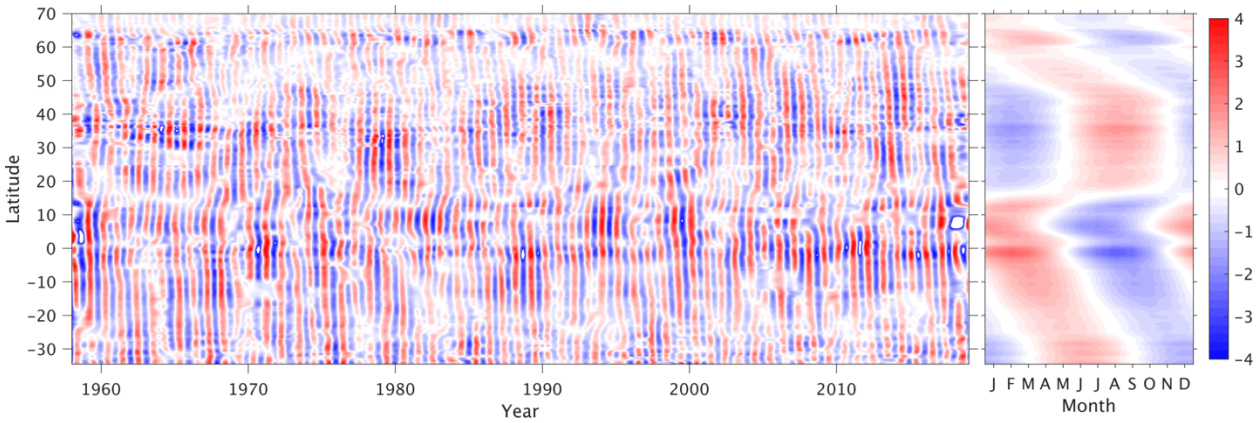

Figure 23. Modeled seasonal variability of the AMOC transport (in Sv) in the Atlantic basin (35°S-70°N), based on the 3rd Intrinsic mode function (IMF) using the ensemble empirical mode decomposition (EEMD,Wu and Huang 2009). The right panel shows the monthly variability averaged over 1958-2018.

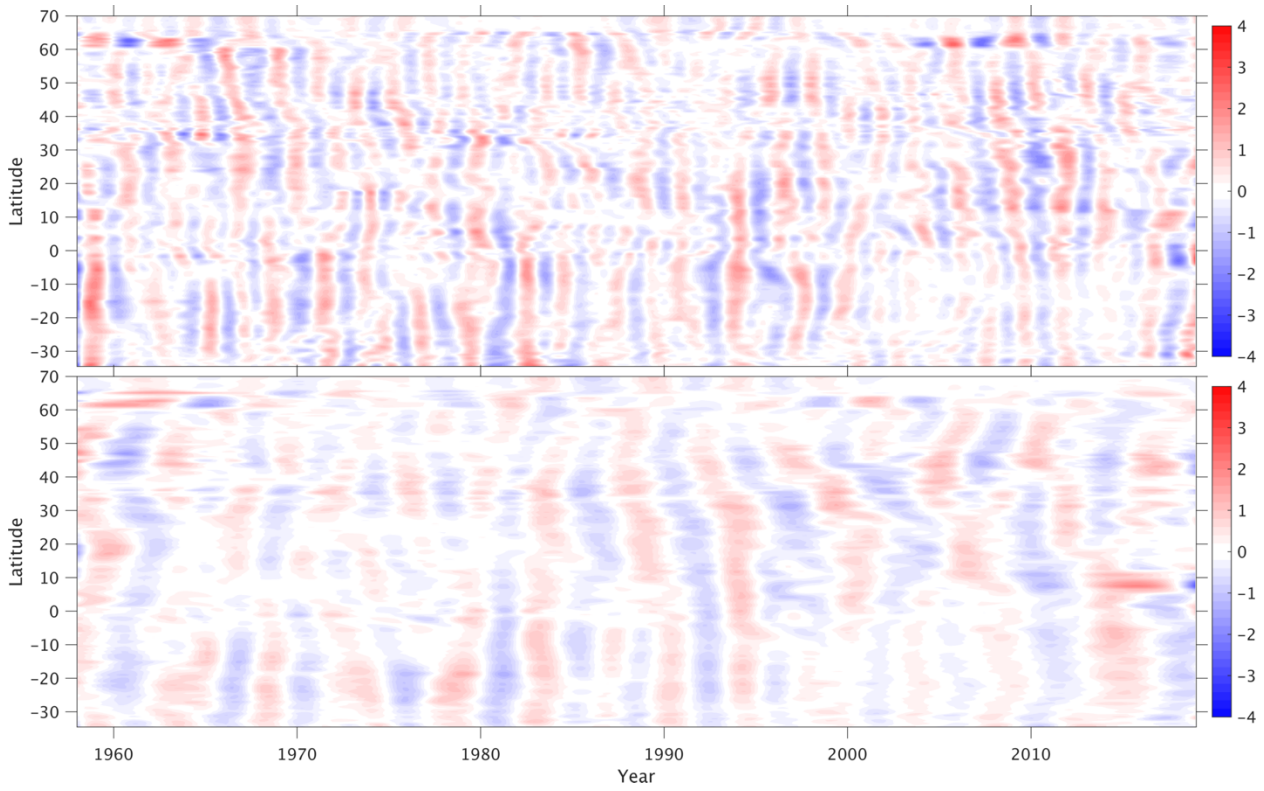

Figure 24. Modeled interannual variability of the AMOC transport (in Sv) in the Atlantic basin (35°S-70°N), based on the 4th and 5th Intrinsic mode function (IMF).

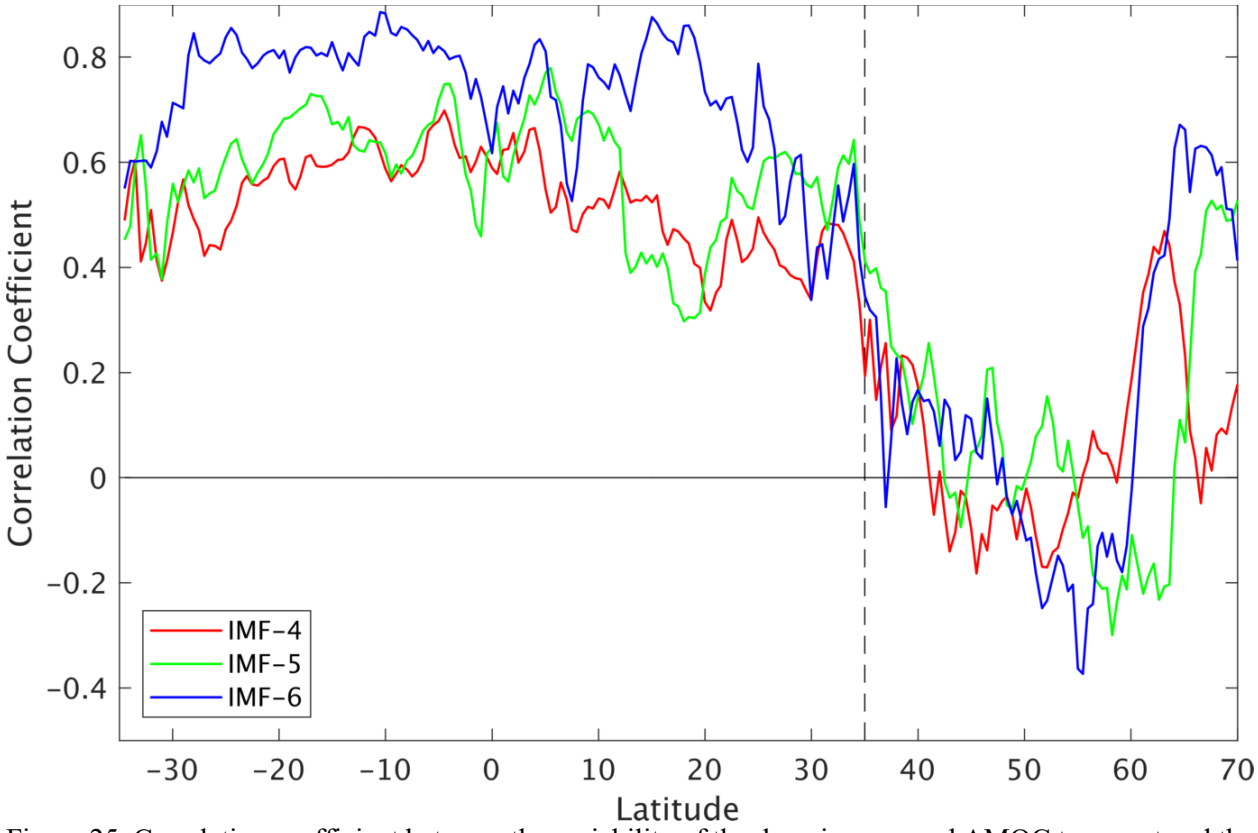

Figure 25. Correlation coefficient between the variability of the domain averaged AMOC transport and the variability of the AMOC transport at each latitude; Red and green are interannual variability (4th and 5th IMF) shown in Figure 24 and blue is decadal variability (6th IMF) shown in Figure 26.

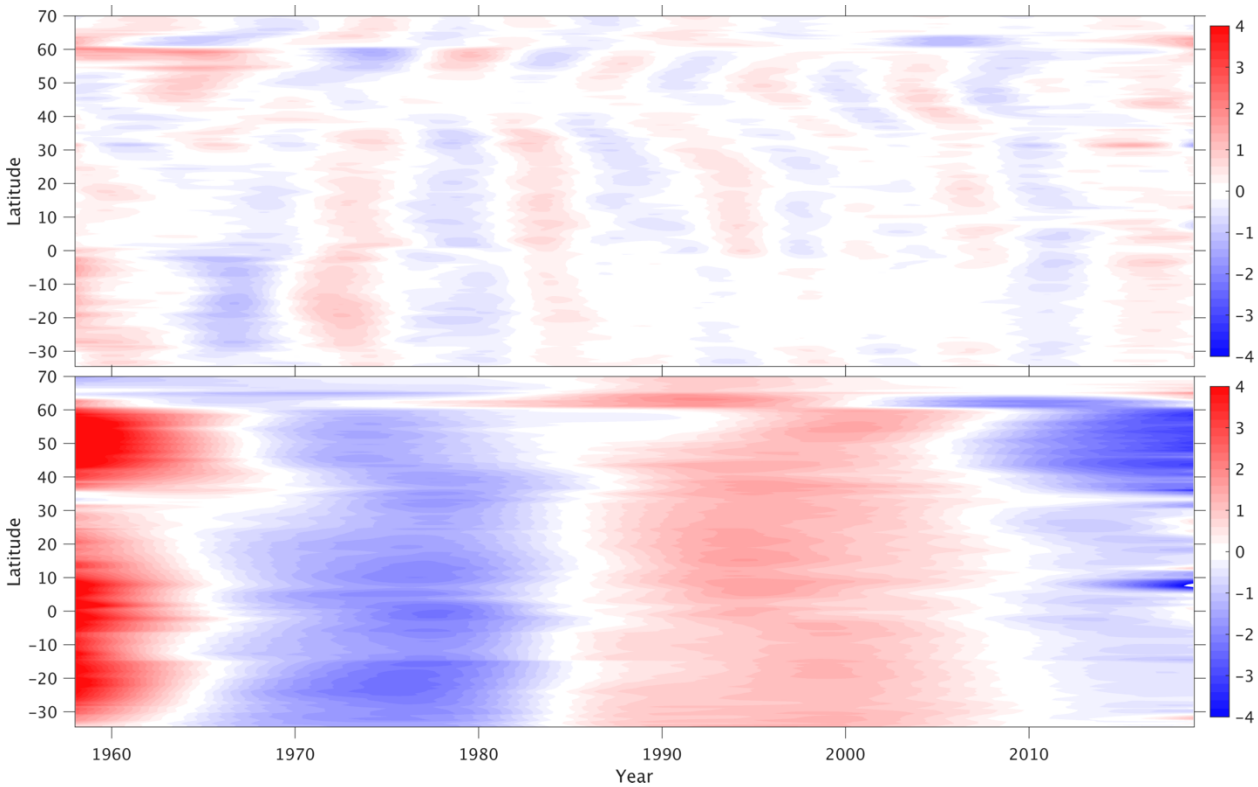

Figure 26. Modeled decadal and longer-term variability of the AMOC transport (in Sv) in the Atlantic Basin (35°S-70°N), based on the 6th and the sum of 7th to 9th Intrinsic mode function (IMF), respectively.